ADVANCING EARTH AND SPACE SCIENCES

JGR Earth Surface

RESEARCH ARTICLE
10.1029/2023JF007193

Impact of Quaternary Glaciations on Denudation Rates in North Pamir—Tian Shan Inferred From Cosmogenic ^{10}Be and Low-Temperature Thermochronology

Anna Kudriavtseva[1,2], Alexandru T. Codilean[2,3], Edward R. Sobel[1], Angela Landgraf[1,4], Réka-H. Fülöp[2,5], Atyrgul Dzhumabaeva[6], Kanatbek Abdrakhmatov[6], Klaus M. Wilcken[5], Taylor Schildgen[1,7], David Fink[5], Toshiyuki Fujioka[5,8], Lingxiao Gong[1], Swenja Rosenwinkel[1], Silke Merchel[9,10], and Georg Rugel[9]

[1]Institute of Geosciences, University of Potsdam, Potsdam-Golm, Germany, [2]School of Earth, Atmospheric and Life Sciences, University of Wollongong, Wollongong, NSW, Australia, [3]ARC Centre of Excellence for Australian Biodiversity and Heritage (CABAH), University of Wollongong, Wollongong, NSW, Australia, [4]NAGRA, Wettingen, Switzerland, [5]Australian Nuclear Science and Technology Organisation (ANSTO), Lucas Heights, NSW, Australia, [6]Institute of Seismology, National Academy of Science of Kyrgyzstan, Bishkek, Kyrgyzstan, [7]GFZ German Research Centre for Geosciences, Potsdam, Germany, [8]Centro Nacional de Investigación sobre la Evolución Humana (CENIEH), Burgos, Spain, [9]Helmholtz-Zentrum Dresden-Rossendorf, Helmholtz Institute Freiberg for Resource Technology, Dresden, Germany, [10]Isotope Physics, Faculty of Physics, University of Vienna, Vienna, Austria

Key Points:

- Modern denudation rates are higher than paleo-denudation rates from 2.0 to 2.7 Ma and exhumation rates inferred from thermochronology
- Denudation in the Terskey range remained steady during the Neogene and early Pleistocene and then increased in the Quaternary after 2.0 Ma
- The denudational response to Quaternary glaciations is detectable in the Kyrgyz and Chinese portions of the Tian Shan

Supporting Information:

Supporting Information may be found in the online version of this article.

Correspondence to:

A. Kudriavtseva,
kudriavtseva.anna.a@gmail.com

Citation:

Kudriavtseva, A., Codilean, A. T., Sobel, E. R., Landgraf, A., Fülöp, R.-H., Dzhumabaeva, A., et al. (2023). Impact of Quaternary glaciations on denudation rates in north Pamir—Tian Shan inferred from cosmogenic ^{10}Be and low-temperature thermochronology. *Journal of Geophysical Research: Earth Surface*, *128*, e2023JF007193. https://doi.org/10.1029/2023JF007193

Received 3 APR 2023
Accepted 8 NOV 2023

Abstract We explore the spatial and temporal variations in denudation rates in the northern Pamir—Tian Shan region using ^{10}Be-derived denudation rates from modern ($n = 110$) and buried sediment (2.0–2.7 Ma; $n = 3$), and long-term exhumation rates from published apatite fission track (AFT; $n = 705$) and apatite (U-Th-Sm)/He (AHe; $n = 211$) thermochronology. We found moderate correlations between denudation rates and topographic metrics and weak correlations between denudation rates and annual rainfall, highlighting complex linkages among tectonics, climate, and surface processes that vary locally. The ^{10}Be data show a spatial trend of decreasing modern denudation rates from west to east, suggesting that deformation and precipitation control denudation in the northern Pamir and western Tian Shan. Farther east, the denudational response of the landscape to Quaternary glaciations is more pronounced and reflected in our data. Modern ^{10}Be denudation rates are generally higher than the long-term AFT and AHe exhumation rates across the studied area. In the Kyrgyz Tian Shan, on average, the highest ^{10}Be denudation rates are recorded in the Terskey range, south of Lake Issyk-Kul. Here, modern denudation rates are higher than ^{10}Be-derived paleo-denudation rates, which are comparable in magnitude with the long-term exhumation rates inferred from AFT and AHe. We propose that denudation in the region, particularly in the Terskey range, remained relatively steady during the Neogene and early Pleistocene. Denudation increased due to glacial-interglacial cycles in the Quaternary, but this occurred after the onset and intensification of the Northern Hemisphere glaciations at 2.7 Ma.

Plain Language Summary Tectonic forces create mountains, while climatically modulated erosion breaks them down into sediment that rivers carry to the final depositional basin. This cycle affects global climate over long periods, but it's unclear whether mountain uplift causes climate change or if climate cooling leads to faster erosion and mountain uplift. To tackle these questions, we explore temporal and spatial changes in rates of denudation in the northern Pamir—Tian Shan region and find that rates remained steady during the Neogene and early Pleistocene but increased due to glacial-interglacial cycles in the Quaternary. We also find that modern denudation rates decrease from west to east. This suggests that tectonic deformation controls denudation in the northern Pamir and western Tian Shan, while further east the denudational response of the landscape to Quaternary glaciations is more pronounced and reflected in our data. Dominant controls on modern denudation rates vary across the mountain range and reflect local factors. Our results highlight how the evolution of mountain belts strongly depends on denudation, which reflects complex interactions between tectonics, climatic changes, and surface processes, and show how in the northern Pamir—Tian Shan region, climate cooling during the Quaternary period resulted in faster erosion rates.

10.1029/2023JF007193

1. Introduction

The evolution of orogens depends on the balance between rock uplift and denudation, which reflects complex interactions among tectonics, climate, and surface processes (e.g., Avouac & Burov, 1996; Burbank et al., 2003; Molnar & England, 1990; Montgomery & Brandon, 2002; Raymo & Ruddiman, 1992; Whipple, 2009). However, these interactions are often interdependent, and their relative importance for denudation is mainly controlled by regional and local conditions (e.g., S. A. Chen et al., 2022; Portenga & Bierman, 2011). Denudation has been argued to either increase with the late Cenozoic onset of the Northern Hemisphere glaciations (S. A. Chen et al., 2022; Herman & Champagnac, 2016; Herman et al., 2018; Mariotti et al., 2021; Molnar, 2004; Norton & Schlunegger, 2017; Shuster et al., 2011; Zhang et al., 2001), or remain steady (Willenbring & Jerolmack, 2016; Willenbring & Von Blanckenburg, 2010). Alternatively, other studies argue that denudation rates are primarily controlled by enhanced tectonic activity (Hecht & Oguchi, 2017; Koppes & Montgomery, 2009) or by post-orogenic isostatic rebound of foreland basins (Bernard & Sinclair, 2022). However, other studies show that late Cenozoic denudation rates are too poorly resolved to determine any global patterns (e.g., Schildgen et al., 2018).

During the Cenozoic, Central Asia experienced extensive tectonic deformation associated with the uplift of the Tibetan Plateau, the Pamir mountains, the Tian Shan, and the Altai mountains (e.g., Molnar & Tapponnier, 1975) as well as dramatic changes in climate associated with the onset of Quaternary glacial-interglacial cycles (Batbaatar et al., 2021; Caves et al., 2016). Moreover, the Tian Shan creates an important topographic barrier to moisture-bearing westerly winds, playing a crucial role in the Cenozoic aridification of Central Asia (e.g., Caves Rugenstein & Chamberlain, 2018).

Studies on the Quaternary denudation in the Pamir (Fuchs et al., 2015; Grin et al., 2018) and the eastern (Chinese) Tian Shan (Charreau et al., 2011, 2017, 2023; Guan et al., 2022; Guerit et al., 2016; Liu et al., 2011; Puchol et al., 2017) shed light on spatial and temporal variations in denudation throughout northern Central Asia (Figure 1), yet denudation within the Kyrgyz part of the Tian Shan, situated between the Pamir and Chinese Tian Shan, has been poorly studied. Available thermochronology data from the Kyrgyz Tian Shan help to constrain exhumation rates averaging over million-year timescales (e.g., Glorie & De Grave, 2016); however, these data are not suitable for evaluating the variability of late-Cenozoic denudation rates following the Plio-Pleistocene onset of Northern Hemisphere glaciations (e.g., Reiners & Brandon, 2006).

Here we present previously unpublished ^{10}Be-derived basin-wide denudation rates from modern river sediment ($n = 54$) from across the Kyrgyz Tian Shan and the Kazakh part of the Trans Ili (Zaili) and Kungey ranges (Kyrgyz data set), as well as ^{10}Be-derived paleo-denudation rates from buried river sediment dated 2.0–2.7 Ma ($n = 3$) from the southern side of the Issyk-Kul basin (Figure 1a). We compare these data to published ^{10}Be-derived basin-wide denudation rates from the western Tian Shan and northern Pamir (Western data set; $n = 20$; Grin et al., 2018) and eastern (Chinese) Tian Shan (Eastern data set; $n = 34$; Charreau et al., 2023), as well as to long-term exhumation rates calculated from published apatite fission track (AFT) ($n = 705$) and apatite (U-Th-Sm)/He (AHe, $n = 211$) thermochronology data from across much of the Tian Shan. We also explore relationships between denudation rates and geomorphic, tectonic, and climatic parameters to identify potential controls on denudation at the regional and local scales. Taken together, these data provide insights into spatial and temporal variations in denudation in the Tian Shan and allow us to untangle the effects of tectonics and climatic changes on denudation across the orogen.

2. Tectonic and Climatic Setting

The Tian Shan is a 2,500-km long intracontinental mountain belt, situated between the Tarim and Tajik basins to the south and the Kazakh platform to the north and extending over the territories of north-western China, Kyrgyzstan, southern Kazakhstan, eastern Uzbekistan, and northern Tajikistan (Figure 1).

The Tian Shan is formed by accretion and collision of oceanic fragments, island arcs, and continental blocks during the Paleozoic, which resulted in the formation of the Northern, Middle, and Southern terranes in the Kyrgyz portion of the Tian Shan (e.g., Bakirov & Maksumova, 2001; Bazhenov et al., 2003; Biske & Seltmann, 2010; Windley et al., 1990, 2007). The terranes are cross-cut by the dextral strike-slip Talas-Fergana Fault and separated by the sinistral strike-slip Nikolaev Line and the Southern Tian Shan Suture (Figure 1a) (Alexeiev et al., 2017;

10.1029/2023JF007193

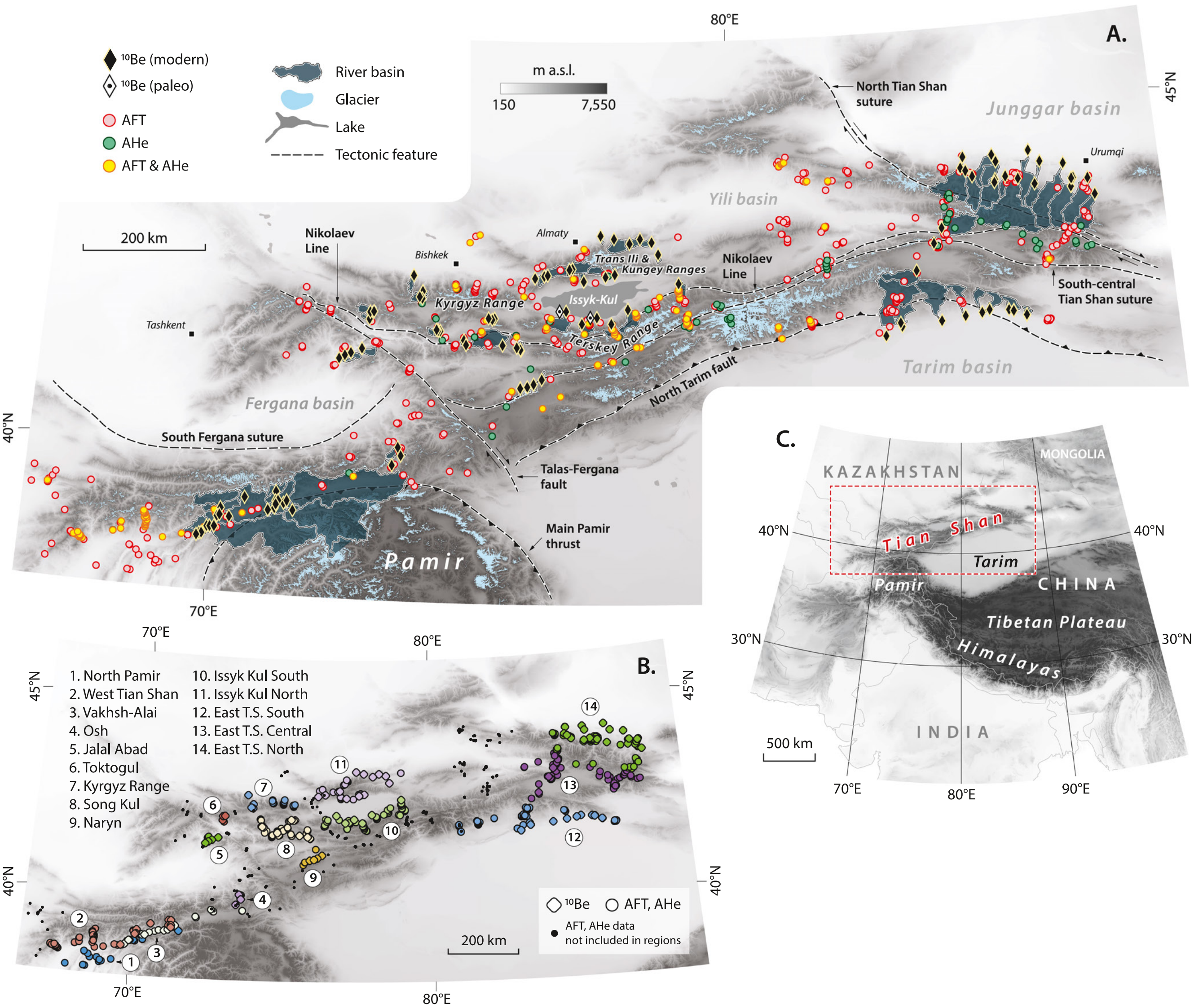

Figure 1. Topographic maps of the Tian Shan based on the 90-m SRTM DEM and distribution of samples. (a) Positions of ^{10}Be, apatite fission track (AFT), and AHe samples across the Tian Shan, distribution of present-day glaciers, and major tectonic structures. Glacier extent based on the Global Land Ice Measurements from Space (GLIMS) database (Raup et al., 2007) and tectonic structures based on H.-D. Li et al. (2022). (b) Distribution of ^{10}Be, AFT, and AHe samples by region within the Tian Shan. Regions 1–3: western Tian Shan and northern Pamir. Regions 4–11: Kyrgyz Tian Shan. Regions 12–14: eastern (Chinese) Tian Shan. (c) Position of the Tian Shan in Central Asia.

Bazhenov & Mikolaichuk, 2004; Glorie et al., 2011). In the Mesozoic and Cenozoic, the Tian Shan was periodically reactivated in response to distal collisions (De Grave, 2003; Hendrix et al., 1992; Jolivet et al., 2010) with an intervening period of tectonic quiescence (Abdrakhmatov et al., 2001; Macaulay et al., 2013).

The present topography of the Tian Shan and the Pamir is a result of crustal shortening triggered by deformation due to the India-Asia collision (Molnar & Tapponnier, 1975). The northward movement of the Pamir and the Tarim block causes shortening and deformation in the Tian Shan, and the Main Pamir Thrust separates the two orogens (Figure 1). Deformation in the Tian Shan started in the late Oligocene at ca. 25 Ma, as indicated by thermochronology, and remained tectonically confined to the major fault zones (Glorie & De Grave, 2016; Sobel, Chen, & Heermance, 2006). Cenozoic shortening in the Tian Shan decreases from south to north and from west to east, deformation progressed out of sequence; associated surface uplift rates varied along the strike (Abdrakhmatov et al., 1996; Bande, Sobel, Mikolaichuk, & Torres Acosta, 2017; Glorie & De Grave, 2016; Glorie et al., 2011; Goode et al., 2014; Macaulay et al., 2014; S. C. Thompson et al., 2002; Zubovich et al., 2010).

10.1029/2023JF007193

North-south shortening and deformation in the Tian Shan intensified at ca. 15–5 Ma and caused widespread thrusting at ca. 10 Ma (e.g., Bande, Sobel, Mikolaichuk, Schmidt, & Stockli, 2017; Bullen et al., 2003; Jolivet et al., 2010; W. Li et al., 2022; Macaulay et al., 2014; Y. Wang et al., 2023; Zubovich et al., 2010). Deformation in the interior ranges possibly intensified at ca. 3–2 Ma (e.g., Glorie et al., 2010, 2011; Goode et al., 2014; Macaulay et al., 2014) mostly in the western and partly in the central parts of the Tian Shan (Y. Wang et al., 2023). The strike slip displacement of the Talas-Fergana Fault commenced at ca. 25 Ma and was relatively rapid until ca. 13.5 Ma (Bande, Sobel, Mikolaichuk, & Torres Acosta, 2017). Quaternary shortening is distributed across the entire Tian Shan and rates are inferred to be similar to modern shortening rates. The most rapid Quaternary shortening documented in the Kyrgyz Tian Shan occurred in the Naryn basin (S. C. Thompson et al., 2002). However, seismicity seems to be concentrated along the northern margin, including a significant series of five large-magnitude earthquakes between 1885 and 1938 (M_w 6.9 to >8) (e.g., Landgraf et al., 2016). The present-day shortening rate is about 20 mm yr^{-1} in the Kyrgyz Tian Shan, which is approximately half of the present-day India-Asia convergence rate (Abdrakhmatov et al., 1996; Zubovich et al., 2010), and 10–15 mm yr^{-1} in the western Tian Shan and in the Pamir (Ischuk et al., 2013; Sippl et al., 2014).

In the Pamir, significant Cenozoic deformation commenced in the Eocene; a second major pulse was recorded in the early Miocene; in the north Pamir, the latter is typically linked to motion along the north-vergent Main Pamir Thrust (Figure 1), which bounds the northern Pamir (e.g., Amidon & Hynek, 2010; Rutte et al., 2017). Deformation migrated to the bounding basins in the middle-late Miocene (e.g., Abdulhameed et al., 2020; J. Thompson et al., 2015). Although there are debates about the magnitude and mechanism of Pamir shortening (e.g., Burtman & Molnar, 1993; Kufner et al., 2016; Y. P. Li et al., 2020), Pamir-Tian Shan convergence is certainly driven by the northward motion of India.

The Cenozoic climate in Central Asia has been arid and mainly influenced by the northern mid-latitude westerlies, which transport moisture eastward across Eurasia (e.g., Caves et al., 2015, 2016). Aridification was likely caused by a decrease in the westerlies' moisture flux, which resulted from Cenozoic global cooling and Parathethys retreat (Miao et al., 2012; Ramstein et al., 1997), as well as the creation of orographic barriers due to surface uplift of the Tibetan Plateau, the Tian Shan, and the Pamir mountains (Caves Rugenstein & Chamberlain, 2018; Kent-Corson et al., 2009; Kudriavtseva et al., 2023; X. Wang et al., 2020). The Tian Shan has interacted with the westerlies since the late Oligocene (X. Wang et al., 2020). In the mid-Pliocene and during Quaternary interglacial periods, northerly migration of the westerlies induced higher precipitation, whereas their southward migration during Quaternary glacial periods led to drier climate conditions (Botsyun et al., 2022).

Modern precipitation in the Tian Shan and the Pamir is controlled by interactions between the westerlies and the Siberian High (V. B. Aizen et al., 1997; Schwarz et al., 2017; Zech, 2012). The westerlies bring moisture from the North Atlantic, the Mediterranean, and the Black Sea (V. B. Aizen et al., 2006; Lauterbach et al., 2014). In winter, the Siberian High reaches the Tian Shan and blocks the midlatitude westerlies, resulting in cold conditions and reduced precipitation (E. M. Aizen et al., 2001; Ricketts et al., 2001). The South and East Asian monsoons never consistently reached the Tian Shan and do not influence precipitation and long-term climate within the range (Caves et al., 2015; Wu et al., 2022). Presently, an orographic barrier created by the range is responsible for the seasonality of precipitation, with dominantly winter-spring precipitation on the windward (north-western) side of the Tian Shan and summer precipitation within the range and on its leeward (south-eastern) side (Baldwin & Vecchi, 2016). This seasonality occurs because during the winter, the prevalent Siberian High and weak westerlies lead to orographic rainout of the westerly moisture on the windward side, while strong cyclonic activity at high elevations in the summer leads to rainfall at high elevations (Bershaw & Lechler, 2019).

Summarizing the above, high topography of the Tian Shan developed during the Neogene due to the India-Asia collision, with the most significant intensification at 15–5 Ma. The range prevents the westerly moisture from reaching the Chinese part of Central Asia, playing a part in aridification.

3. Materials and Methods

3.1. Cosmogenic ^{10}Be Analysis

Cosmogenic ^{10}Be produced in quartz has proven to be the best suited technique for studying the denudation of Earth's continental topography over millennial timescales (Schaefer et al., 2022). Indeed, ^{10}Be-based denudation rates have now been determined in more than 4,000 river basins—mostly from mountain landscapes—providing us with a large inventory of denudation rate estimates (Codilean et al., 2018, 2022). The concentration of ^{10}Be nuclides in river sediments is proportional to their exposure age, with the highest ^{10}Be concentrations reflecting longer exposure time and, consequently, slower denudation (Granger & Schaller, 2014; Schaefer et al., 2022).

3.1.1. Sampling

We collected 54 modern river sediment samples to calculate ^{10}Be-derived millennial-scale basin-wide denudation rates (Figure 1a and Figure S1 in Supporting Information S1, Table S1 in Supporting Information S2). Sampling was performed in locations across Kyrgyzstan accessible by road with the purpose of covering the largest possible area of the Kyrgyz Tian Shan and covering several catchments in individual ranges, if possible. River sediment was sieved in the field to isolate the 250–500 µm fraction for analysis. At two sampling locations we also collected material in the 8–16 mm (samples KYR16-01B and KYR16-02B) and 16–32 mm (sample KYR16-01C) grain size ranges. Sampling of buried sediments for calculation of ^{10}Be-derived paleo-denudation rates and calculation of ages using isochron burial dating (Figure 1a, Table S2 in Supporting Information S2) are described in Kudriavtseva et al. (2023). Our sample inventory includes one modern river sediment sample (KYR-DRMS1) previously reported by Landgraf et al. (2016).

3.1.2. Sample Preparation

Quartz was purified following the procedures described in Kohl and Nishiizumi (1992) using froth flotation to separate feldspars from quartz. For all samples except those labeled "DRMS" in Table S1 in Supporting Information S2, beryllium was separated at the University of Wollongong (UOW) following procedures described in Codilean et al. (2023). Samples were spiked with ≈300 µg of ^{9}Be from a low-level beryllium carrier solution added prior to complete HF dissolution. ^{10}Be/^{9}Be ratios were measured using the 10 MV ANTARES accelerator (samples with cathode ID's in Table S1 starting with "B" in Supporting Information S2) and using the 6 MV SIRIUS accelerator (samples with cathode ID's in Table S1 starting with "Be" and "XBE" in Supporting Information S2) at the Australian Nuclear Science and Technology Organisation (ANSTO) (Fink & Smith, 2007; Wilcken et al., 2017, 2019, 2022), and were normalized to the KN-5-2 and KN-5-3 (Nishiizumi et al., 2007) standards. Analytical uncertainties for the final ^{10}Be concentrations (atoms g^{-1}) include AMS measurement uncertainties (the larger of counting statistics or standard deviation of repeats and blank corrections) in quadrature with 1%–2% for ^{10}Be standard reproducibility (depending on the individual AMS measurement conditions) and 1% uncertainty in the ^{9}Be carrier concentration. Samples labeled "DRMS" were prepared and analyzed at the DREAMS facility at Helmholtz-Zentrum Dresden Rossendorf (Rugel et al., 2016).

3.1.3. Denudation Rates From Modern Samples

We used the open-source program CAIRN v.1 (Mudd et al., 2016) to calculate denudation rates from our Kyrgyz samples, and to recalculate published denudation rates from Grin et al. (2018) and Charreau et al. (2023). Basin-averaged nuclide production from neutrons and muons was calculated with the approximation of Braucher et al. (2011) and using a sea-level and high-latitude total production rate of 4.3 atoms g^{-1} yr^{-1} for ^{10}Be (Mudd et al., 2016). Production rates for catchment-wide denudation rates were calculated at every grid cell of a hydrologically enforced 90-m SRTM DEM (Farr et al., 2007) using the time-independent Lal/Stone scaling scheme (Stone, 2000). Atmospheric pressure was calculated via interpolation from the NCEP2 reanalysis data (Compo et al., 2011). For consistency with the denudation rates compiled in the OCTOPUS database (Codilean et al., 2018, 2022), we applied topographic shielding corrections to our data. The latter was calculated from the same DEM using the method of Codilean (2006) with $\Delta\theta = 8°$ and $\Delta\phi = 5°$. For completeness and in line with DiBiase (2018), we also calculate denudation rates without correcting for topographic shielding. The uncorrected denudation rates are provided in Tables S1 in Supporting Information S2 and overlap with those corrected for topographic shielding at 1σ uncertainty.

In mountain regions, not accounting for snow or glacier ice shielding will result in an overestimation of ^{10}Be-derived denudation rates (Granger & Schaller, 2014; Schaefer et al., 2022). The lack of detailed meteorological data on snow thickness from the study area prevents us from rigorously correcting our denudation rates for snow shielding. To determine whether not accounting for snow shielding could bias our denudation rates, we calculate snow shielding-corrected denudation rates assuming an average annual snow depth of 5 cm (equivalent to 20 cm over the winter months) uniformly covering the surface of each sampled basin. This snow depth value is equivalent to the maximum mean snow depths recorded in the Tian Shan over the last century (Q. Li et al., 2019) and thus represents an upper limit. End-member snow-depth corrected denudation rates are about 8% lower than the uncorrected ones and the two overlap at 1σ uncertainty. Actual snow shielding values are lower than our assumed end-member case, and thus, not accounting for snow shielding has minimal impact on the reported denudation rates (Table S1 in Supporting Information S2). Given the lack of meteorological data required for rigorous snow shielding corrections, and given that both topographic shielding and snow shielding corrections have minimal impact on the obtained denudation rates, and for consistency with denudation rates compiled in the OCTOPUS database (Codilean et al., 2018, 2022), in subsequent analyses we use denudation rates that were corrected for topographic shielding but not corrected for snow shielding.

Due to the presence of glaciers in the study area we also explore the potential impact of present and past glaciations on the inferred ^{10}Be denudation rates. To this end, we calculate end-member ^{10}Be denudation rates for the entire ^{10}Be data set using present-day glacier extents mapped in the Global Land Ice Measurements from Space (GLIMS) database (Raup et al., 2007; Stroeven et al., 2013) by assuming that glaciated areas contribute with sediment in proportion to their surface areas and that this sediment has a ^{10}Be concentration of zero. Stroeven et al. (2013) have mapped the extent of glaciated valleys throughout the Kyrgyz section of the Tian Shan, and we use these data to calculate end-member ^{10}Be denudation rates for our Kyrgyz data accounting for the maximum extent of Quaternary glaciations. Similar to our present-day glacier calculations, we assume that the sediment sourced from glaciated valleys have ^{10}Be concentrations equal to zero. Results are summarized in Table S1 in Supporting Information S2 and discussed below.

3.1.4. Paleo-Denudation Rates From Buried Samples

Paleo-denudation rates were calculated using three buried amalgamated sand samples (250–500 μm grain size) from south of lake Issyk-Kul (Figure 1a), taken from the same stratigraphic layers as the individual clasts collected for isochron burial dating by Kudriavtseva et al. (2023). The ^{26}Al and ^{10}Be concentrations measured in the sand samples plot near (sample AKT) or intersect (samples PET-QTS) the lines defined by the isochron clast samples (Figure S2 in Supporting Information S1), indicating that the sands and clasts have experienced similar exposure and burial histories. We calculate paleo-denudation rates by first correcting the ^{10}Be concentrations measured in the sand samples for radioactive decay using the isochron burial ages calculated for each location (see Table S2 in Supporting Information S2 and Kudriavtseva et al., 2023). To account for uncertainties related to the average elevation of the sediment's source areas and to the possibility of incomplete burial or lengthy exposure to cosmic radiation prior to sampling, we express paleo-denudation rates for each of the three localities as a range of values in addition to a central value obtained by assuming complete and continuous burial (Table S2 in Supporting Information S2).

3.2. AFT and AHe Thermochronology

Thermochronology is used to reconstruct the time at which rocks cooled through a temperature window, which allows the estimation of the timing and rate of exhumation for rocks that are currently at the surface (e.g., Reiners & Brandon, 2006). Different thermochronological systems have different closure temperatures (dependent on mineral used or decay scheme targeted), and different closure temperatures result in different averaging timescales of exhumation. The temperature windows for the AFT and AHe systems are 60–120 and 40–85°C, respectively, and the typical closure temperatures are 110 and 70°C, respectively (e.g., Reiners & Brandon, 2006).

To estimate long-term exhumation rates across the Tian Shan, we compile AFT ($n = 705$, Table S3 in Supporting Information S2) and apatite (U-Th-Sm)/He (AHe, $n = 211$, Table S4 in Supporting Information S2) ages available in the published literature (see Tables S3 and S4 in Supporting Information S2 for list of publications). We calculate one-dimensional, steady-state exhumation rates from the published AFT and AHe cooling ages using the *age2exhume* MATLAB code (Van der Beek & Schildgen, 2023).

The *age2exhume* code incorporates surface temperature based on a defined mean annual temperature at sea level (T_0) and a temperature lapse rate. Using mean annual temperature values for the Tian Shan from the WorldClim Global Climate database (Fick & Hijmans, 2017), we estimate a value for T_0 of 19°C. Based on values estimated for the Chinese Tian Shan (Shen et al., 2016), we assume a temperature lapse rate of 5°C km^{-1}. To explore the sensitivity of the calculated exhumation rates to our choices of T_0 and lapse rate, we also calculated exhumation rates using T_0 = 15°C and 25°C, and lapse rates of 4 and 4.5°C km^{-1} (Tables S3 and S4 in Supporting Information S2). The average difference in obtained exhumation rates for a change in T_0 from 15 to 25°C is 11% for AFT and 21% for AHe (Figure 2), and for a change in the lapse rate from 4 to 5°C km^{-1} the differences are 2.6%

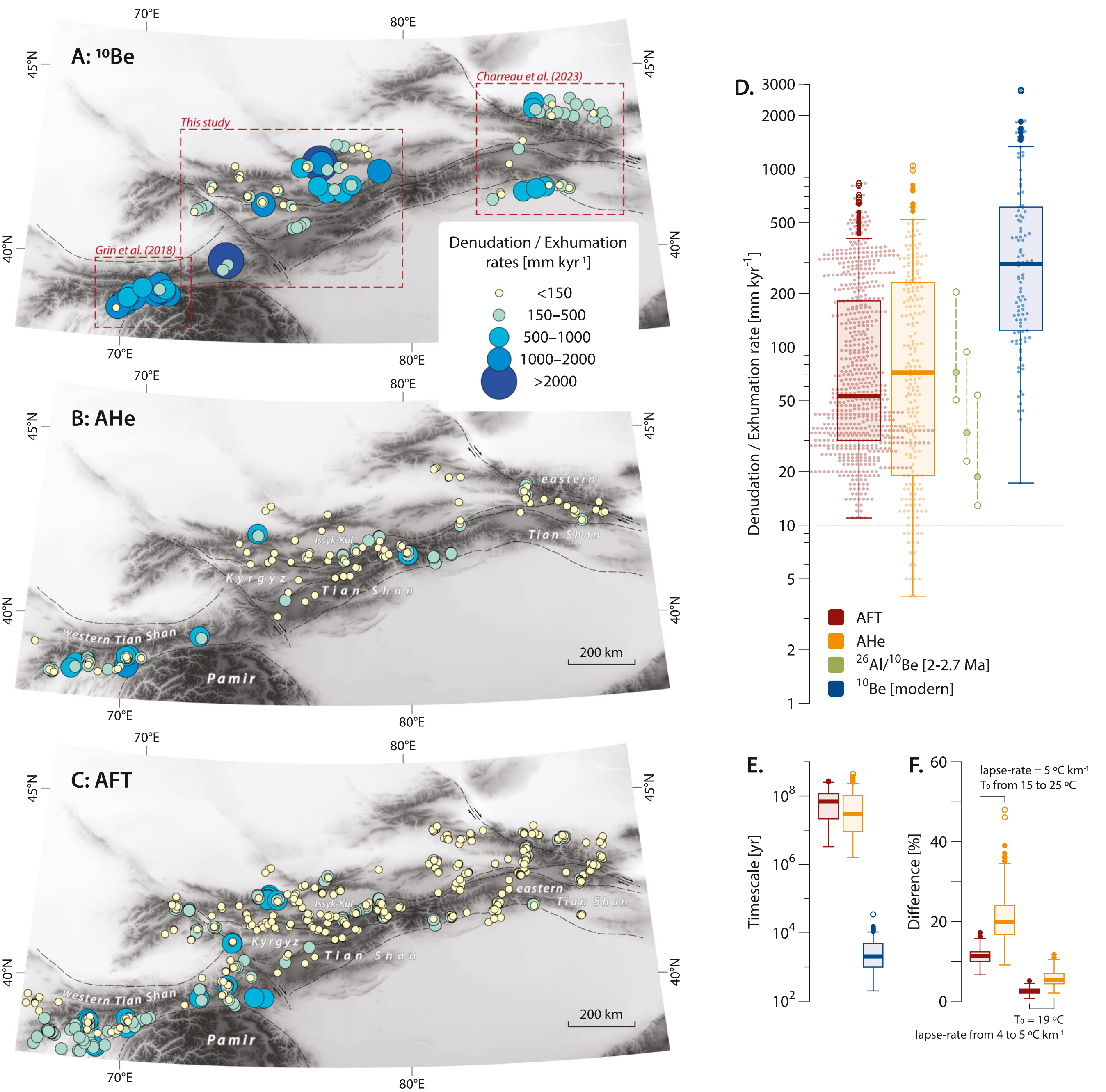

Figure 2. Summary of ^{10}Be, apatite fission track (AFT), and AHe results. (a)–(c) Spatial distribution of modern ^{10}Be-derived denudation rates (a), and AHe (b) and AFT (c) exhumation rates. Black dashed lines show the location of major tectonic features (see Figure 1 for more details). (d) Interquartile-range (IQR) box and whisker plots showing AFT and AHe exhumation rates, and modern ^{10}Be-derived denudation rates from across the Tian Shan. (e) Averaging timescales for the AFT, AHe and ^{10}Be denudation/exhumation rates shown in (d). (f) Percent differences between AFT and AHe exhumation rates modeled using different values for T_0 and temperature lapse-rate, respectively.

and 5.7% for AFT and AHe, respectively (Figure 2). Given the orders-of-magnitude range in exhumation rates (and denudation rates) explored here, the above differences are not significant. We set the initial geotherm to 25°C km^{-1}; as required to initiate the model, but a steady-state geotherm is calculated for each sample as the model runs (see Van der Beek & Schildgen, 2023). We assume a (default) thermal diffusivity of 30 km^2 Myr^{-1}, and a model thickness of 30 km. Model results are not sensitive to the assumed model thickness (see sensitivity tests in Van der Beek & Schildgen, 2023); this value was chosen as a rough estimate of the starting thermal field for the model, which encompasses typical depths from which rocks were tectonically exhumed in the Tian Shan.

Kinetic parameters for the AHe system are derived from Farley (2000) and for the AFT system from Reiners and Brandon (2006). A local relief correction, Δh, for each sample is calculated based on the difference between the sample elevation and a smoothed version of the modern topography that approximates the relief on the closure-temperature isotherm (for details, see Van der Beek & Schildgen, 2023). To calculate a smoothed version of the DEM from which Δh values are derived, the 90-m resolution SRTM DEM was smoothed over a circular radius equal to 70 pixels (6,300 m) for the AHe system, and 105 pixels (9,450 m) for the AFT system. These distances are equivalent to assuming a closure depth (z_c) of ca. 2 km for the AHe system, and ca. 3 km for the AFT system, with a smoothing radius equal to $\pi * z_c$ (Willett & Brandon, 2013). The Δh values for each sample (modern elevation minus smoothed DEM) are included in Tables S3 and S4 in Supporting Information S2. Our approach assumes exhumational steady state and neglects track length data, which is not available for many AFT samples. For AFT samples with pre-Cenozoic ages, our simplifying assumptions likely overestimate the exhumation rates; however, the rates calculated from these samples are already quite low.

We acknowledge that for sites with both AFT and AHe data, it would be possible to model the data together to obtain more accurate exhumation histories, but for the purposes of this study, in which we simply aim to explore how exhumation rates change over time, we opted for an approach that could be rapidly and consistently applied to all samples.

3.3. Geomorphic, Climatic, and Tectonic Parameters

To explore potential environmental controls on ^{10}Be-derived denudation rates, we calculate the average of various geomorphic, tectonic, and climatic metrics for each drainage basin (Figure 3). For geomorphic metrics, we use a hydrologically enforced 90-m SRTM DEM (Farr et al., 2007). We calculate the topographic gradient using the algorithm proposed by Horn (1981), and we calculate local relief as the elevation range within a moving circular window with a radius of 2 km. We calculated the normalized channel steepness index (k_{sn}) with the Topographic Analysis Kit for the TopoToolbox MATLAB package (Forte & Whipple, 2019; Schwanghart & Kuhn, 2010; Schwanghart & Scherler, 2014) using the *KsnChiBatch* tool with the reference concavity set to 0.5 and with the *output* parameter set to "*ksn*" and a stream network basin area threshold of 1 km^2. The latter produces a stream network with k_{sn} values for each stream segment, as opposed to a continuous raster with interpolated k_{sn} values. We use these raw stream network k_{sn} values as opposed to an interpolated k_{sn} raster to calculate our summary statistics for each basin. As metrics for climate, we use the bioclimatic variables available as part of the WorldClim Global Climate database (Fick & Hijmans, 2017), namely BIO12 (mean annual rainfall) and BIO13 (rainfall of the wettest month), and the global aridity index (AI) map (Zomer et al., 2022). As a metric for tectonic deformation, we use data from the Global Strain Rate Model (Kreemer et al., 2014). The extracted metrics are summarized in Tables S5A and S5B in Supporting Information S2. Lastly, we extract the dominant lithological units for each basin using the Global Lithological Map (GLiM) database (Hartmann & Moosdorf, 2012) and present the results in Figure S3 in Supporting Information S1.

3.4. Data Grouping

To facilitate a meaningful comparison between the ^{10}Be-derived denudation rates and the long-term exhumation rates inferred from the published AFT and AHe data, we divide our Kyrgyz ^{10}Be data set into eight regions (Figures 1b and 2, Figure S1 in Supporting Information S1, Table S5 in Supporting Information S2): Issyk-Kul North (n = 14), Issyk-Kul South (n = 8), Song Kul (n = 13), Naryn (n = 5), Kyrgyz range (n = 4), Toktogul (n = 3), Jalal Abad (n = 4), and Osh (n = 3). The grouping strategy is focused on the regional distribution of our modern sediment ^{10}Be data. The published denudation rates from Grin et al. (2018) and Charreau et al. (2023) are divided into regions proposed by the corresponding authors. In each region we include AFT and AHe datapoints that are located within, or in the proximity, of the drainage basins with ^{10}Be data and belong to the same tectonic position (e.g., footwall/hanging wall). In total data are grouped into 14 regions, shown in Figure 1b.

4. Results

The ^{10}Be concentrations of modern river sands in the Kyrgyz Tian Shan range between 7.92 ± 0.83 × 10^3 and 1,460.12 ± 29.24 × 10^3 atoms g^{-1} (Table S1 in Supporting Information S2 and Figure 2). Basin-wide denudation rates calculated from these concentrations ranged between 17.3 and 2,780.4 mm kyr^{-1} (uncorrected for

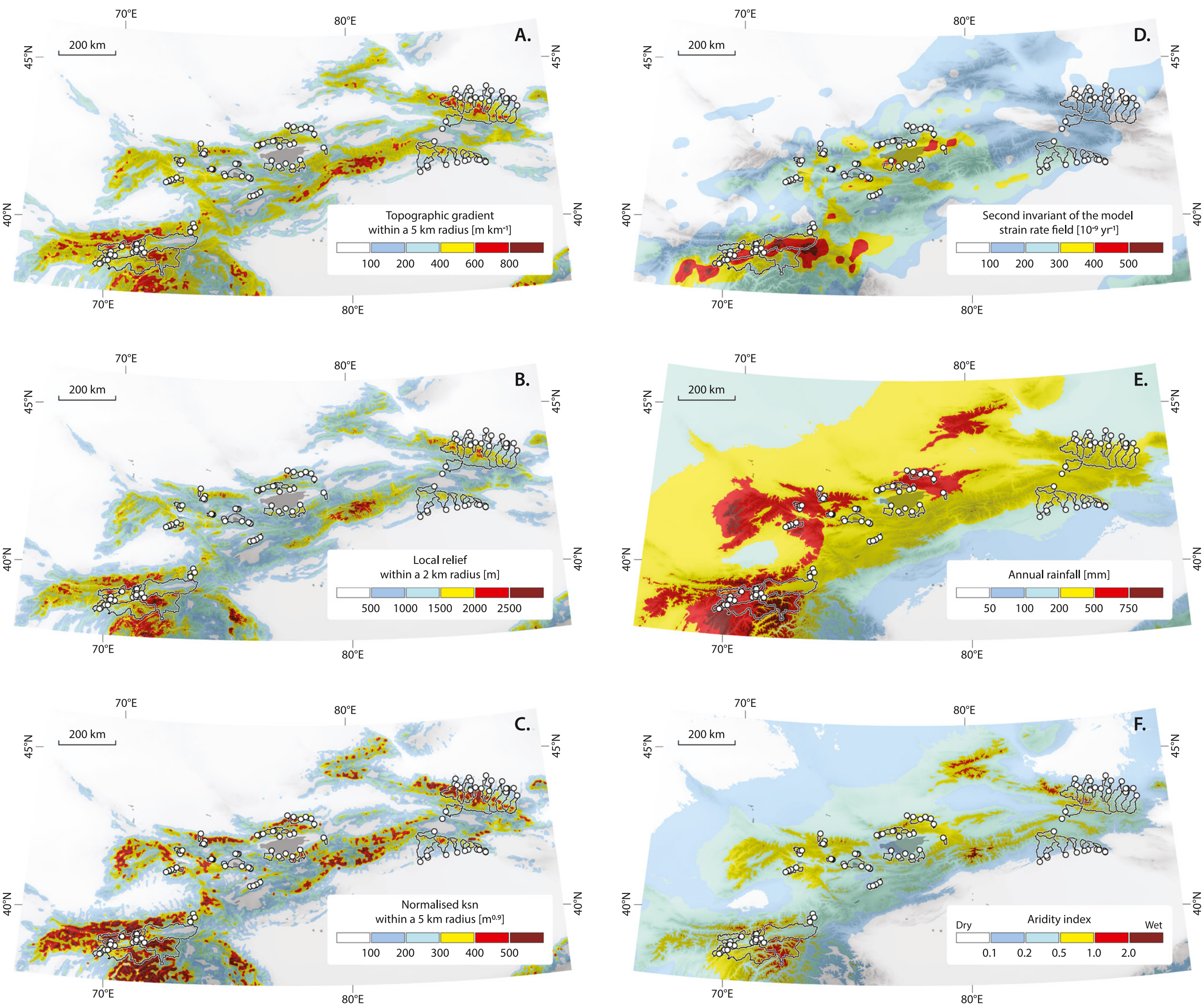

Figure 3. Maps showing the spatial distribution of topographic, tectonic, and climatic metrics across the Tian Shan. Topographic gradient (a), local relief (b), and normalized channel steepness—ksn (c) were calculated using the 90-m SRTM DEM (Farr et al., 2007). For clarity of the maps, the topographic gradient and normalized ksn are shown as average values within a 5 km radius moving window. The second invariant of the model strain rate field (d) was obtained from the Global Strain Rate Model (Kreemer et al., 2014), annual rainfall (e) was obtained from the WorldClim Global Climate database (Fick & Hijmans, 2017), and the aridity index (f) was obtained from Zomer et al. (2022).

modern glacial cover), with a mean value of 393.8 mm kyr^{-1} and a median value of 179.6 mm kyr^{-1} (Tables S1 and S6 in Supporting Information S2). Averaging time range between 15.3 and 0.2 kyr, with one outlier value of 34.8 kyr (sample KYR16-39) in the Song Kul region (Figures 2a and 2e; Tables S1 and S5A in Supporting Information S2). Recalculated ^{10}Be-derived denudation rates from the western Tian Shan and northern Pamir ranged between 142.3 and 1,861.8 mm kyr^{-1}, with a mean value of 1,234.8 mm kyr^{-1} and a median value of 1,391.8 mm kyr^{-1}, and averaging times between 0.3 and 4.2 kyr (Figures 2a and 2e; Table S5B in Supporting Information S2). Recalculated ^{10}Be-derived denudation rates from the eastern (Chinese) Tian Shan range between 43.8 and 743.2 mm kyr^{-1}, with the mean value of 274.2 mm kyr^{-1} and median value of 243.6 mm kyr^{-1}, and averaging times between 0.8 and 13.7 kyr (Figures 2a and 2e; Table S5B in Supporting Information S2). Correcting for the maximum impact of present-day glaciers yields end-member basin-wide denudation rates that are on average 21% lower than the uncorrected values (Tables S1, S5A, and S5B in Supporting Information S2), however this difference has negligible impact on the overall distribution of denudation rates and on their comparison to the AFT- and AHe-derived exhumation rates (Figures 4 and 5).

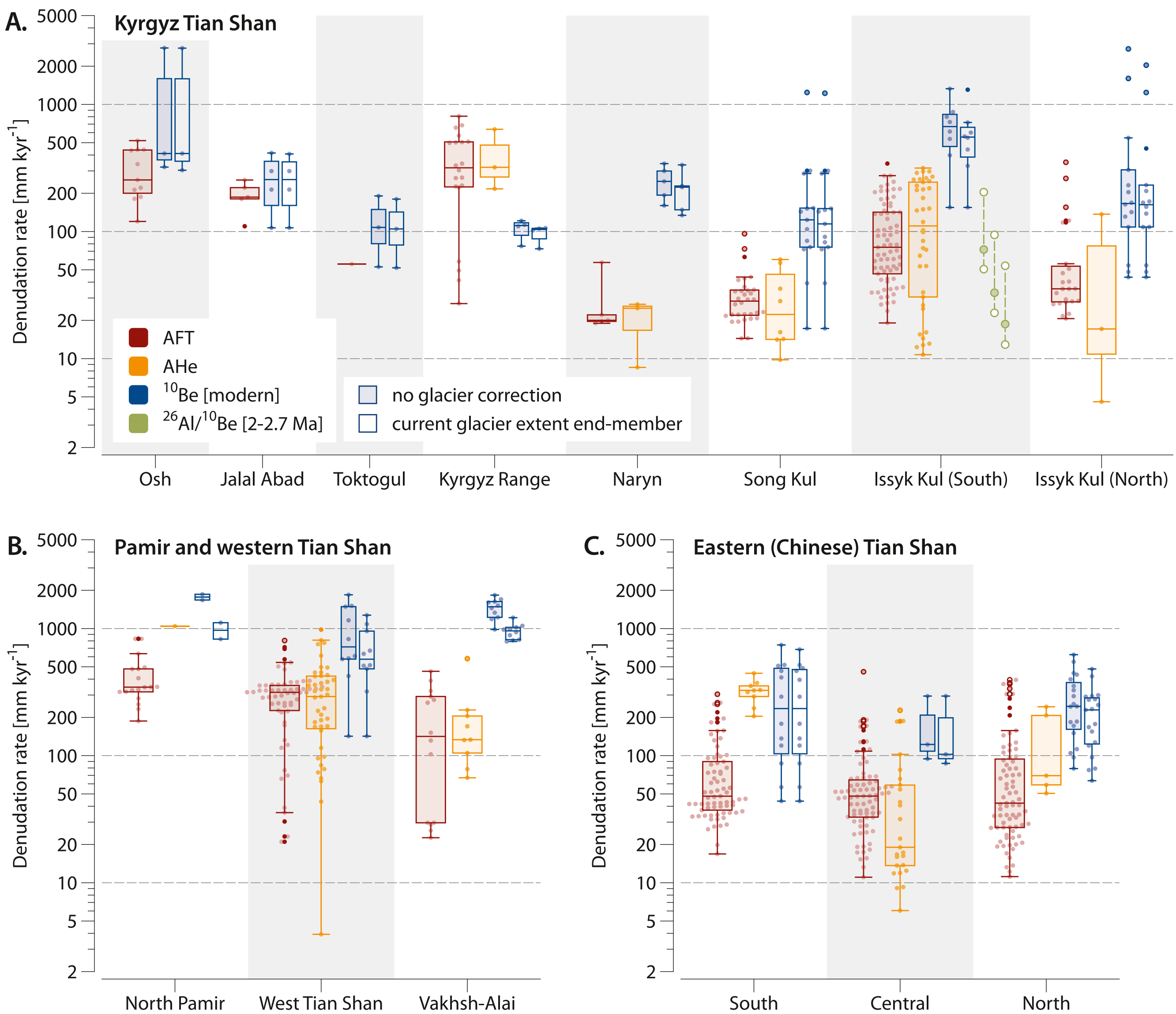

Figure 4. Interquartile-range (IQR) box and whisker plots showing apatite fission track and AHe exhumation rates, and ^{10}Be-derived modern and paleo-denudation rates for (a) the Kyrgyz Tian Shan, (b) northern Pamir and western Tian Shan, and (c) eastern (Chinese) Tian Shan. Blue box plots with no fill show end-member ^{10}Be-derived modern denudation rates corrected for the maximum effect of present-day glacier cover on diluting the ^{10}Be-signal exported by rivers from each sampled drainage basin (see text for details).

The cosmogenic nuclide concentrations, ages, and paleo-denudation rates of buried samples from the southern part of the Issyk-Kul basin are shown in Figure 4 and Table S2 in Supporting Information S2. The ^{10}Be and ^{26}Al concentrations ($\times 10^3$ atoms g^{-1}) of the buried samples are as follows: 30.80 ± 1.01 and 57.34 ± 6.56 (^{10}Be and ^{26}Al respectively, AKT-U); 92.04 ± 2.53 and 272.15 ± 16.11 (PET-QTS-L); and 114.78 ± 3.16 and 227.15 ± 17.31 (PET-QTS-PIT). Paleo-denudation rates (mm kyr^{-1}) obtained by assuming complete and continuous burial are 72.2 ± 11.7 (AKT-U; burial age = 2.71 ± 0.37), 33.0 ± 3.5 (PET-QTS-L; burial age = 2.08 ± 0.14), and 18.7 ± 1.8 (PET-QTS-PIT; burial age = 2.75 ± 0.15). Allowing for uncertainties related to the average elevation of the sediment's source areas and to the possibility of incomplete burial or lengthy exposure to cosmic radiation prior to sampling, we obtain the following paleo-denudation rate ranges for the three sites: 50.6 ± 8.2–204.0 ± 32.8 for AKT-U; 22.9 ± 2.5–94.1 ± 10.0 for QTS-L; and 12.9 ± 1.2–53.8 ± 5.1 for QTS-PIT.

The calculated long-term AFT and AHe exhumation rates from the entire Tian Shan are summarized in Figures 2 and 4 and in Tables S3 and S4 in Supporting Information S2. Inferred AFT exhumation rates (T_0 = 19°C, lapse rate = 5°C km^{-1}) range between 11.1 and 831.4 mm kyr^{-1}, and inferred AHe exhumation rates (T_0 = 19°C,

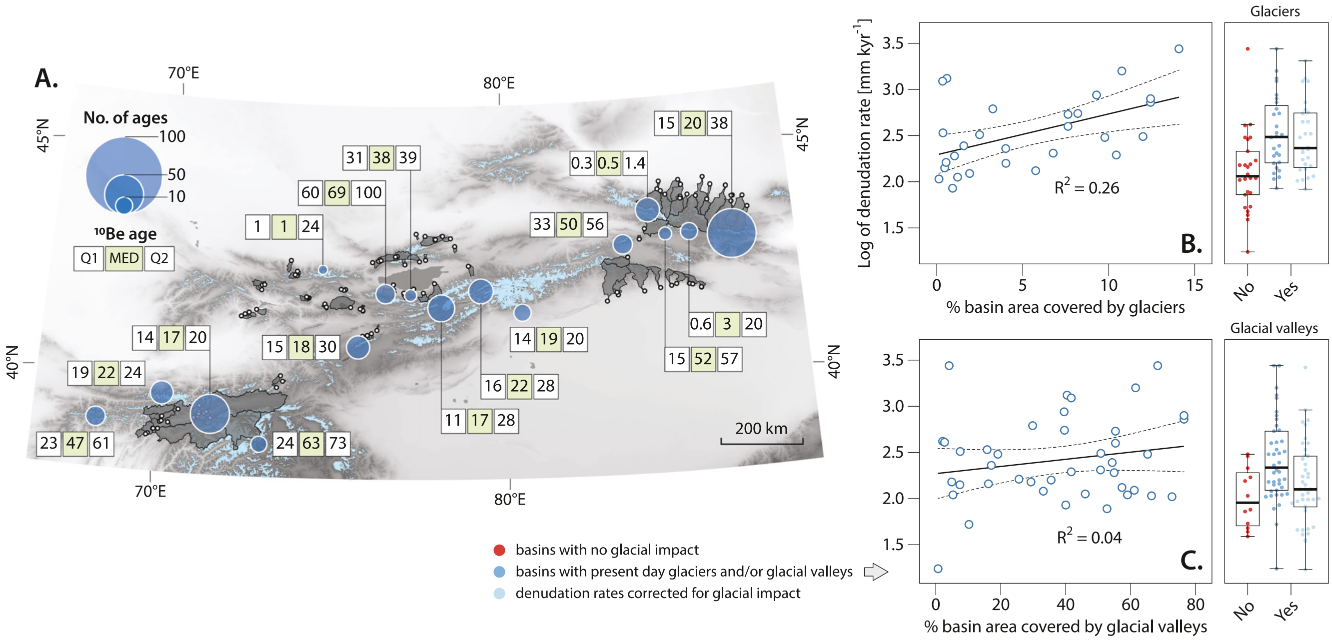

Figure 5. Deglaciation ages in the Tian Shan and links between ^{10}Be-derived modern denudation rates and modern and past glaciers. (a) Map summarizing ^{10}Be-derived deglaciation ages across the Tian Shan obtained from the ExpAge database (https://expage.github.io). Ages are grouped in clusters based on their geographic locations (blue circles) and for each cluster the map lists the median age (MED; green box) and the interquartile-range (Q1 and Q2 respectively). The size of circles is proportional to the number of ages within each cluster. (b) and (c) Log-transformed ^{10}Be denudation rate versus percentage of basin area covered by present-day glaciers (b) and glacial valleys (c). Box plots summarize log-transformed denudation rates for basins with no glacial impact (red circles) and basins with glacier impact (blue circles).

lapse rate = 5°C km^{-1}) range between 3.9 and 1,044.2 mm kyr^{-1}. The compiled AFT and AHe data that are not included in the 14 regions (see Section 3.4 above) are still used for the calculation of the mean and median values for the Kyrgyz, Western, and Eastern data sets (see Figure 2d). Mean and median AFT/AHe exhumation rates in the Kyrgyz data set are 212.0 and 96.0 mm kyr^{-1}/94.1 and 39.4 mm kyr^{-1}, respectively. Mean and median AFT/AHe exhumation rates in the Western data set are 268.3 and 291.9 mm kyr^{-1}/300.4 and 227.0 mm kyr^{-1}, respectively. Mean and median AFT/AHe exhumation rates in the Eastern data set are 69.4 and 41.7 mm kyr^{-1}/110.7 and 41.9 mm kyr^{-1}, respectively. The mean and median values for the ^{10}Be-derived millennial-scale denudation rates, AFT-, and AHe-derived long-term exhumation rates for each of the regions are summarized in Table S6 in Supporting Information S2.

When considering the entire ^{10}Be data set, we found moderate but statistically significant (at $p < 0.001$) correlations between the log-transformed ^{10}Be-derived modern denudation rates and topographic metrics (elevation, topographic gradient, and local relief) and strain rate ($R \approx 0.5$; Figure 6). Weak, but still statistically significant correlations are obtained between the log-transformed ^{10}Be-derived modern denudation rates and normalized channel steepness ($R \approx 0.3$; $p < 0.001$), and between the log-transformed rates and rainfall (annual and wettest month) ($R \approx 0.2$; $p < 0.05$) and the AI ($R \approx 0.3$; $p < 0.01$) (Figure 6). At the intermediate scale, the North Pamir and western Tian Shan data sets show a strong correlation between the log-transformed ^{10}Be-derived denudation rates and elevation ($R \approx 0.8$; $p < 0.001$), and a moderate correlation between log-transformed rates and the rainfall of the wettest month and the AI ($R \approx 0.6$; $p < 0.01$) (Figure 6). The Kyrgyz data set shows statistically weak but significant correlations between the log-transformed ^{10}Be-derived denudation rates and topographic metrics (topographic gradient and local relief) ($R \approx 0.4$; $p < 0.001$) and a weak correlation between log-transformed rates and mean annual rainfall ($R \approx 0.3$; $p < 0.05$) (Figure 6). In the eastern (Chinese) Tian Shan, correlations are moderate between the log-transformed ^{10}Be-derived denudation rates and topographic metrics ($R \approx 0.5$; $p < 0.001$), and weak but still statistically significant between log-transformed rates and climatic metrics ($R \approx 0.4$; $p < 0.05$) (Figure 6). At the regional scale, the picture becomes more complicated with correlations between denudation rate and predictors likely reflecting local conditions (Table S7 in Supporting Information S2), and a strong influence of the reduced sample counts. Only seven of the 14 regions have sufficient sample numbers to justify a correlation analysis, and even here the low sample counts likely bias the results.

10.1029/2023JF007193

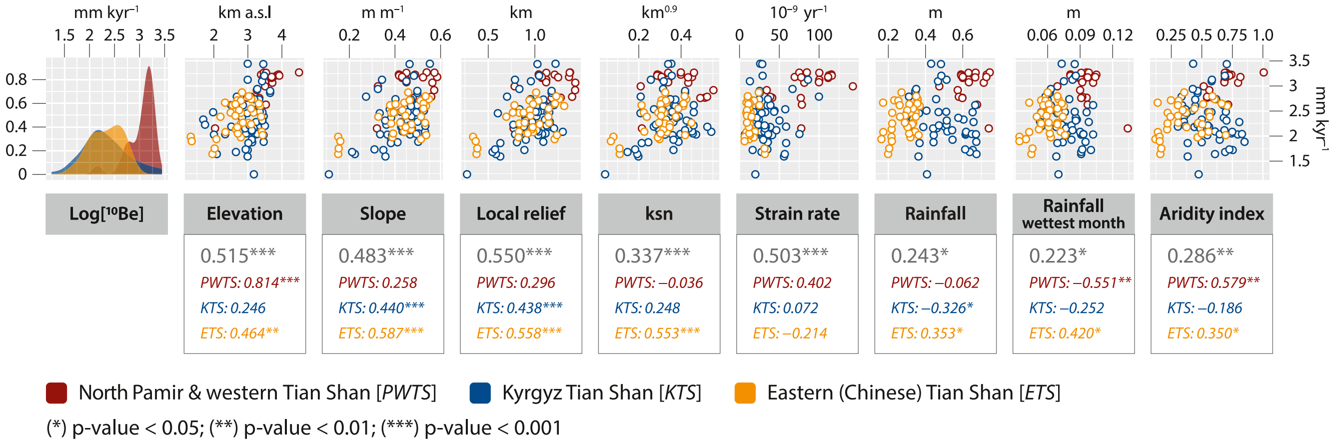

Figure 6. Correlation matrix displaying Pearson's correlation coefficients for ^{10}Be-derived denudation rates and different topographic, tectonic, and climatic metrics calculated for data from northern Pamir and western Tian Shan (Grin et al., 2018), the Kyrgyz Tian Shan (this study), and the eastern (Chinese) Tian Shan (Charreau et al., 2023).

The absence of detailed geology maps for the entire study area prevents us from completing a detailed assessment of potential lithological controls on ^{10}Be-derived denudation rates. However, using the GLiM database (Hartmann & Moosdorf, 2012), we found no correlation between denudation rates and the dominant major lithological units of the sediments' source areas (Figure S3 in Supporting Information S1).

5. Discussion

5.1. The Impact of Present-Day Glaciers on Denudation Rates in the Tian Shan

Alpine glacial cover may impact cosmogenic ^{10}Be abundances via two mechanisms: (a) excavation of material from depth, and (b) shielding of bedrock from cosmic radiation. Both mechanisms lead to a decrease in ^{10}Be concentration in the sediment mix exiting a glaciated drainage basin, and consequently, can result in an overestimation of ^{10}Be-derived denudation rates (Granger & Schaller, 2014; Schaefer et al., 2022). Based on the GLIMS database (Raup et al., 2007), present-day glaciers occupy about 3% of the land surface area of the Tian Shan and 79 of the 110 drainage basins included in this study (72%) are glaciated.

Concerning the timing and extent of past glaciations, a re-evaluation of existing cosmogenic nuclide exposure ages from the Tian Shan (Figure 5a) by Blomdin et al. (2016) suggests that the only well-constrained regional glacial expansion occurred during Marine Isotope Stage (MIS) 2 (29–14 ka; Lisiecki & Raymo, 2005), with glacier extent restricted to valley glaciation due to aridity (Blomdin et al., 2016 and references therein). The largest glacial cover during this time developed in the eastern part of the Kyrgyz Tian Shan (Blomdin et al., 2016). Glacial deposits from the central Kyrgyz and eastern Chinese Tian Shan have apparent minimum ages overlapping with MIS 3 and MIS 5 (29–57 and 71–130 ka, respectively; Lisiecki & Raymo, 2005) (Figure 5), however, given the paucity of the data and/or the poor resolution of the dating, any attempts at correlating regional scale glacial chronologies beyond MIS 2 are speculative (Blomdin et al., 2016).

In the Kyrgyz Tian Shan, drainage basins with present-day glaciers, and those that are currently ice-free but were glaciated in the past (i.e., basins hosting glacial valleys) record on average higher ^{10}Be-derived modern denudation rates than those basins that were never glaciated (Figures 5b and 5c). Given the relatively short averaging timescales characterizing our ^{10}Be denudation rates (average = 3.5 kyr and median = 2.1 kyr) as compared to the "ages" of the glacial valleys (at least MIS 2; Figure 5a), it is unlikely that elevated denudation rates are the result of glacial valleys contributing sediment depleted in ^{10}Be and therefore diluting the ^{10}Be signal exported by rivers. Rather, a more likely cause of the apparent elevated ^{10}Be-derived denudation rates in these basins is the coincidence of glacial valleys with higher elevations, steeper topographic gradients, and higher local reliefs (Figure S4 in Supporting Information S1).

Unlike glacial valleys, there is evidence to suggest that the presence of modern glaciers in a basin does influence the ^{10}Be-derived denudation rate inferred for that basin. For example, in the Kyrgyz Tian Shan, there seems to be a correlation between the log-transformed ^{10}Be denudation rate and the percentage of basin area occupied by modern glaciers (Figure 5b). Furthermore, relatively high ^{10}Be-derived denudation rates in the Issyk-Kul South region (Figure 4) compared to other sampled regions in the Kyrgyz Tian Shan suggest increased denudation of the northern flank of the Terskey range. The reason for these elevated rates, however, is unclear. This region receives a low amount of precipitation (Figure 3e, Table S5A in Supporting Information S2), it is not dissimilar to other regions in terms of topography, and exhumation rates in the Terskey range did not increase after 5 Ma (Macaulay et al., 2014). Presently, the northern peripheral ranges of the Tian Shan, including the Terskey range, are experiencing severe glacier shrinkage (Kutuzov & Shahgedanova, 2009; Sorg et al., 2012). The Terskey range receives most of precipitation in summer, when rainout occurs at high elevations (Bershaw & Lechler, 2019), during which time streams probably transport sediments from previously glaciated areas of the drainage basins. Also, the Tian Shan drainage basins with a higher portion of glaciated area, especially the northern slope of the Terskey range, show a substantial increase in runoff due to glacier reduction (Unger-Shayesteh et al., 2013 and references therein). Additionally, the strong positive correlation between ^{10}Be-derived denudation rates and precipitation of the wettest month (Table S7 in Supporting Information S2) indicates that river runoff might be amplified by summer rainout despite the generally low precipitation. Therefore, relatively high ^{10}Be-derived denudation rates in the Issyk-Kul South region may reflect an increase in denudation due to higher summer runoff, possibly combined with admixing of previously shielded sediments with lower ^{10}Be concentration.

It is not possible to accurately correct every single ^{10}Be-derived denudation rate for the likely dilution effect of modern glaciers on the ^{10}Be concentrations exported from basins, but it is possible to estimate the maximum effect by calculating end-member ^{10}Be denudation rates by assuming that: (a) each glaciated portion of a basin contributes with sediment to the total mix exported in proportion to its surface area, and (b) that this sediment is completely depleted in ^{10}Be. Modern-glacier corrected end-member ^{10}Be denudation rates are on average 21% lower than the uncorrected values (interquartile range between 7% and 31%). However, when denudation rates are amalgamated in the various regions for comparison with the AFT and AHe exhumation rates (Figure 4), differences are insignificant for all but two regions, namely the North Pamir and Vakhsh-Alai, where the corrected and uncorrected data sets have non-overlapping interquartile ranges (Figure 4b). Notwithstanding these differences, end-member ^{10}Be-derived denudation rates are still significantly higher than their respective AFT and AHe exhumation rates. In light of the above, we suggest that our uncorrected ^{10}Be denudation rates are generally not significantly overestimated, especially in the Kyrgyz and eastern (Chinese) Tian Shan.

5.2. Temporal Changes in Denudation Rates in the Kyrgyz Tian Shan

5.2.1. Increase of the Denudation Rates in the Terskey Range (Kyrgyz Tian Shan) After the Onset of Quaternary Glaciations

Denudation/exhumation rates derived from AFT, AHe, and ^{10}Be have very different averaging timescales. More recent rapid exhumation results in younger AFT and AHe cooling ages and faster exhumation rates, while old ages show that the majority of exhumation occurred long ago and that recent exhumation was minor or slow. Ultimately, averaging timescales for AFT and AHe are equal to the measured cooling age, and the resulting exhumation rates represent an average for the entire period of exhumation (Figure 2e). ^{10}Be-derived denudation rates are averaged over the period necessary to erode about 60 cm of surface rock (or 100 cm of sediment), which in tectonically active landscapes are usually on the order of several thousand years. Therefore, our comparison of AFT, AHe, and ^{10}Be data relies on the fact that different thermochronology-derived exhumation rates and ^{10}Be-derived denudation rates reflect a recent change in denudation rates in comparison to a long-term general denudational trend.

Ganti et al. (2016) suggested that in glaciated areas—such as our study area—there is a time-dependent bias of higher denudation rates toward the present with shorter averaging time scales caused by the discrete nature of erosional processes. Their model shows that when using a power law distribution, erosional hiatuses result in a systematic increase in denudation rates toward the present and this mechanism might be invoked to explain the observed increase in ^{10}Be-derived modern denudation rates as compared to the long-term AFT- and AHe-derived exhumation rates. However, the difference between our modern denudation rates and the ^{10}Be-derived paleo-denudation rates—that are also similar in magnitude to the AFT- and AHe-derived rates—suggests that the observed temporal increase in denudation rates in the Kyrgyz Tian Shan is real rather than an artifact of differing averaging timescales.

Sample AKT-U, in the south-western part of the Issyk-Kul basin, dated to 2.71 ± 0.37 Ma (Kudriavtseva et al., 2023), yields a paleo-denudation rate between 50.6 ± 8.2–204.0 ± 32.8 mm kyr^{-1}, whereas the nearest modern river sediment sample (KYR16-05) yields a rate of 612.1 ± 112.8 mm kyr^{-1}. Farther east, samples PET-QTS-L (2.08 ± 0.14 Ma) and PET-QTS-PIT (2.75 ± 0.15 Ma) (Kudriavtseva et al., 2023) yield paleo-denudation rates between 22.9 ± 2.5–94.1 ± 10.0 and 12.9 ± 1.2–53.8 ± 5.1 mm kyr^{-1}, respectively, which are lower than those obtained from the nearest modern river sediment samples: 154.7 ± 28.6 mm kyr^{-1} (KYR16-03), 871.9 ± 158.8 mm kyr^{-1} (KYR16-55), 727.0 ± 131.3 mm kyr^{-1} (KYR16-01B), and 798.17 ± 144.31 mm kyr^{-1} (KYR16-01C) (Tables S1 and S2 in Supporting Information S2). The elevated ^{10}Be-derived modern denudation rates compared to both the 2.0–2.7 Ma ^{10}Be-derived paleo-denudation rates and the long-term AFT and AHe exhumation rates indicate that in the Terskey range of the Kyrgyz Tian Shan, denudation remained relatively steady until an increase in the Quaternary, after ca. 2 Ma.

The Northern Hemisphere glaciations initiated in the Pliocene (Westerhold et al., 2020) and intensified after 2.7 Ma (Hayashi et al., 2020; Ruggieri et al., 2009), but our 2.0–2.7 Ma ^{10}Be-derived paleo-denudation rates from the southern side of the Issyk-Kul basin do not seem to reflect these global climatic changes. Furthermore, thermochronological data suggest that the Terskey range (situated on the southern side of the Issyk-Kul basin; Figure 1a) formed in the Miocene and did not experience strong deformation and exhumation afterward (Macaulay et al., 2014). The strongest glacial erosional response to Quaternary glaciations is predicted by numerical modeling to occur in regions with extensive glaciations, moderate rock uplift rates (i.e., 0.3–1 mm per year), and a wet climate, whereas in arid regions, the response time of glacial erosion is predicted to be long and of small magnitude (Herman et al., 2018). Given the above, we propose that the aridity of the Tian Shan has dampened and delayed the denudational response to climatic forcing and that the Quaternary glacial-interglacial cycles played a primary role in increasing millennial-scale denudation rates in the Kyrgyz Tian Shan and particularly in the Terskey range.

5.2.2. Implications of the Onset of Plio-Pleistocene Glaciations in the Kyrgyz Tian Shan

The similarity in magnitudes between the 2.08 Ma and 2.7 Ma ^{10}Be-derived paleo-denudation rates and the long-term AFT and AHe exhumation rates implies a relatively steady denudation throughout the Miocene, Pliocene, and early Pleistocene. The three samples used to determine our ^{10}Be-derived paleo-denudation rates were collected from rare and thin fine-grained lenses in conglomerates from the Sharpyl Dak sedimentary group, which was deposited above finer-grained sediments and is analogous to the Xiyu formation conglomerates in the Chinese Tian Shan (Abdrakhmatov et al., 2001; J. Chen et al., 2002; Heermance et al., 2007). The deposition of the Sharpyl Dak and Xiyu conglomerates is diachronous across the Tian Shan, varying from mid-Miocene to Pleistocene (Charreau et al., 2009; J. Chen et al., 2002; Heermance et al., 2007; Kudriavtseva et al., 2023), and is considered to mark either the intensification of tectonic activity or the onset of Plio-Pleistocene glaciation in the region (Zhao et al., 2021). Samples AKT-U (2.71 ± 0.37 Ma) and PET-QTS-PIT (2.75 ± 0.15 Ma) were taken from the basal parts of the conglomerates, whereas sample PET-QTS-L (2.08 ± 0.14 Ma) was collected from the youngest outcropping Sharpyl Dak conglomerates (Kudriavtseva et al., 2023). Therefore, the commencement of the deposition of the Sharpyl Dak conglomerates was synchronous with the global intensification of Northern Hemisphere glaciation at 2.7 Ma (Hayashi et al., 2020; Ruggieri et al., 2009). Nevertheless, despite the transition from fine-grained to conglomerate deposition, our data do not indicate an acceleration of denudation at 2.7 Ma.

In the Tian Shan, denudation is generally slow due to arid conditions, despite tectonic activity, high relief, and glaciations (Guerit et al., 2016; Jepson et al., 2021). The absence of a denudational response to the Plio-Pleistocene onset of glaciations inferred from our data may indicate that significant glaciation in the Terskey range of the Kyrgyz Tian Shan only initiated after 2 Ma, or that the onset of Plio-Pleistocene glaciations did not cause a detectable increase in denudation rates. Determining which of the two explanations is more likely is complicated by poor constraints on the onset of glaciations in the Tian Shan (see Blomdin et al., 2016 and discussion above), although there is evidence suggesting that glaciations there occurred asynchronously with those in Europe and North America (Koppes et al., 2008; Sanhueza-Pino et al., 2011). It is important to note that the ^{10}Be-derived paleo-denudation rates reported here are likely not representative of the entire Kyrgyz Tian Shan, but rather reflect local conditions of the Terskey range (Figure 1a). For example, Charreau et al. (2011) reported a ^{10}Be-derived erosional pulse from 3.0 to 1.7 Ma in the eastern (Chinese) Tian Shan, suggesting a transient increase in denudation in response to the onset of Quaternary glaciations. However, this conclusion is based only on data from a single drainage basin. Conversely, Puchol et al. (2017) reported ^{10}Be-derived paleo-denudation

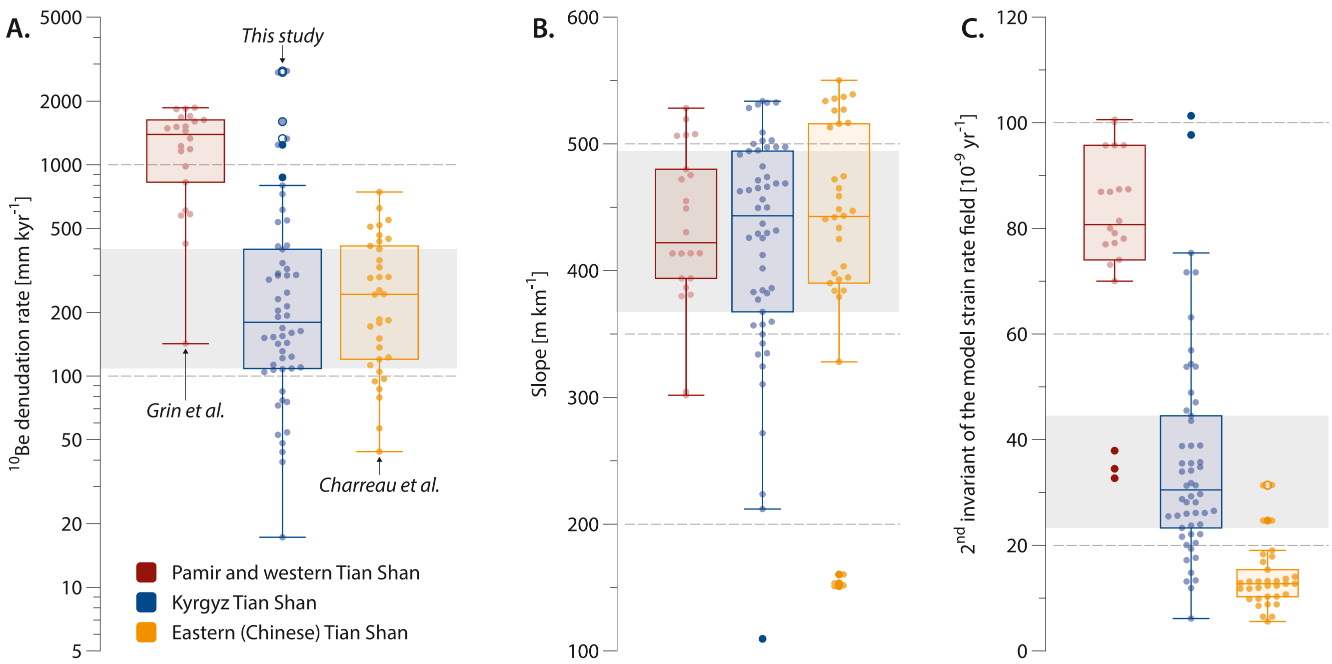

Figure 7. Interquartile-range (IQR) box and whisker plots showing modern ^{10}Be-derived denudation rates, topographic gradient, and strain rate from northern Pamir and western Tian Shan (Grin et al., 2018), the Kyrgyz Tian Shan (this study), and the eastern (Chinese) Tian Shan (Charreau et al., 2023). The horizontal gray bands highlight the IQRs for the Kyrgyz data.

rates from four localities in the eastern (Chinese) Tian Shan, indicating that denudation continuously increased in 9 Ma and remained relatively steady since 4 Ma (i.e., since before the onset of glaciations). Additionally, Puchol et al. (2017) found an increase in the spatial and short-term (<1 Myr) temporal variability of denudation rates between 3 and 1 Ma, suggesting a transient response of the landscape to glacial-interglacial cycles.

Taken together, the above evidence suggests that the erosional response and adjustment of the landscape to the onset of Plio-Pleistocene glaciation may vary spatially and temporally across the Tian Shan. Furthermore, each studied drainage basin may be affected by local tectonic processes. However, it is intriguing that the recent sequence of large magnitude earthquakes in the Kyrgyz, Kungey, and Trans Ili ranges (Landgraf et al., 2016) does not seem to be specifically reflected within the modern ^{10}Be-derived denudation rates.

5.3. Spatial Differences in Denudation/Exhumation Rates in the Tian Shan

5.3.1. West to East Decrease in Denudation/Exhumation Rates Across the Tian Shan

Comparison of our Kyrgyz ^{10}Be data with the Western (Grin et al., 2018) and the Eastern (Charreau et al., 2023) data sets illustrates a west to east trend of decreasing average ^{10}Be-derived modern denudation rates (Figures 2 and 7). A similar decreasing west to east trend is also observed in the AFT and AHe data, yet the ^{10}Be-derived denudation rates remain higher than AFT and AHe across the Tian Shan (Figure 2). Elevated exhumation and denudation rates and notably higher strain rates in the western Tian Shan and northern Pamir most likely reflect strong deformation caused by the northward motion of the Pamir (Figure 7c; Y. Wang et al., 2023). High denudation rates might also be sustained by higher precipitation because the Pamir acts as a topographic barrier to the westerlies (Figure 3e; Carrapa et al., 2014; X. Wang et al., 2020; Richter et al., 2022). Conversely, in the eastern (Chinese) Tian Shan, exhumation and denudation rates are relatively low (Figure 7) and denudation rates stayed relatively steady since at least the Pleistocene (Charreau et al., 2011, 2017, 2023). Geodetically determined north-south shortening rates decrease eastward within the Tian Shan (Zubovich et al., 2010). Taken together, the available data suggest that strong tectonic activity and higher precipitation rates exert a pronounced control on denudation in the northern Pamir and western Tian Shan, whereas further east, precipitation and tectonically driven denudation decrease and the denudational response of the landscape to Quaternary glaciations becomes detectable.

5.3.2. Kyrgyz Range—Outlier Region in the Kyrgyz Tian Shan

The exhumation of the Kyrgyz range, the only area in the Tian Shan showing modern ^{10}Be-derived denudation rates that are lower than exhumation rates derived from thermochronology, commenced at 11–7 Ma and propagated eastward (Bullen et al., 2001, 2003; Sobel, Oskin, et al., 2006). Before that time, this area was a basin filled with ca. 2 km of young, relatively poorly consolidated sediments. For this reason, elevated AFT exhumation rates recorded for the Kyrgyz range likely represent rapid exhumation of these poorly consolidated sediments at the beginning of the range growth (Bullen et al., 2003; Sobel, Oskin, et al., 2006). ^{10}Be-derived modern denudation rates in the Kyrgyz range are similar to those recorded in other Kyrgyz regions (Figure 4a), suggesting a deceleration of denudation after removal of the poorly consolidated sediments and a subsequent adjustment of denudation rates to the glacial conditions across the Kyrgyz Tian Shan.

5.4. Influence of Topographic, Tectonic, and Climatic Factors on ^{10}Be-Derived Denudation Rates

When considering the entire ^{10}Be data set, our analyses reveal weak but statistically significant correlations between log-transformed ^{10}Be-derived modern denudation rates and climatic metrics (precipitation and AI), and moderate correlations with strain rate (expressed as the second invariant of the model strain rate field; Kreemer et al., 2014) and topographic metrics (Figure 6). However, the pattern changes when considering the three data sets (namely (a) norther Pamir and western Tian Shan, (b) Kyrgyz Tian Shan, and (c) eastern (Chinese) Tian Shan) separately (Figure 6) and the regions within them (Table S7 in Supporting Information S2). The three data sets exhibit stronger correlations with topographic metrics and weaker correlations with climatic metrics. Both the Kyrgyz and the eastern (Chinese) Tian Shan data sets show moderate correlations with slope and relief and weak correlations with annual rainfall. Western and eastern Tian Shan data sets show moderate (western) and weak (eastern) correlations with precipitation of the wettest month and AI. Elevation is a strong predictor in the western Tian Shan data set and only moderate in the eastern one. The normalized channel steepness (k_{sn}) is a moderate predictor only in the eastern Tian Shan data set. Among separate regions, a strong correlation is observed only between denudation rates in the western Tian Shan and topographic gradient. The majority of other regions show moderate and weak correlations with topographic metrics, and several regions have weak correlations with climatic metrics (Table S7 in Supporting Information S2).

The above likely reflects moderate but primary tectonic and topographic control on denudation rates in general across the Tian Shan and both strong deformation and high precipitation rates in the Pamir. Interestingly, in the Issyk-Kul South region (Terskey range of the Kyrgyz Tian Shan), denudation rates only show a statistically significant correlation with the precipitation of the wettest month and AI, implying that denudation in the Terskey range is primarily controlled by summer rainfall despite the generally low amount of precipitation. This pattern is notably different from other regions of the Tian Shan, where topographic metrics are more significant predictors than climatic ones. The lack of a strong correlation between denudation rates in separate regions and topographic metrics is not unusual, considering the complex interplay among surface processes, tectonics, and climate (S. A. Chen et al., 2022; Dosseto & Schaller, 2016; Portenga & Bierman, 2011). This result is consistent with findings by Grin et al. (2018) in the western Tian Shan and northern Pamir and Charreau et al. (2023) in the eastern (Chinese) Tian Shan—both studies reported weak correlations between ^{10}Be denudation rate and topographic metrics. Furthermore, our analysis found no statistically significant correlation between denudation rates in the three data sets and separate regions and strain rate (expressed as the second invariant of the model strain rate field; Kreemer et al., 2014).

The lack of strong correlation and the variability in dominant predictors between regions is not surprising and is likely explained by the large spatial spread of our ^{10}Be data set—especially in the Kyrgyz Tian Shan—and the influence of local factors. Despite a relatively large ^{10}Be sample count ($n = 110$), due to the large spatial spread of the data set, the individual groups (Figure 1b) have relatively few ^{10}Be data points, some too few to even warrant correlation analyses. It is likely that even in the relatively larger groups for which we did undertake correlation analyses (i.e., those included in Table S7 in Supporting Information S2), outliers may have too much influence on the obtained correlation coefficients. For this reason, correlation analyses are included here for their heuristic value and need to be interpreted with caution.

6. Conclusions

We report ^{10}Be-derived basin-wide denudation rates from modern river sediment from across the Kyrgyz Tian Shan and the Kazakh part of the Trans Ili and Kungey ranges, as well as ^{10}Be-derived paleo-denudation rates from buried river sediment dated to 2.0–2.7 Ma from the southern side of the Issyk-Kul basin. We compare these data to published ^{10}Be-derived basin-wide denudation rates from the western Tian Shan and northern Pamir and eastern (Chinese) Tian Shan, as well as long-term exhumation rates, calculated from published AFT and apatite (U-Th-Sm)/He (AHe) thermochronology data from this entire region, and explore the spatial and temporal variations in denudation rates in the Tian Shan and northern Pamir as well as relationships between denudation rates and geomorphic, tectonic, and climatic metrics to identify potential controls on denudation at the local scale.

Our results show that the ^{10}Be-derived denudation rates obtained from modern river sediment are generally higher than long-term AFT and AHe exhumation rates across the entire study area, except for the Kyrgyz range (Figures 2 and 4). There, ^{10}Be-derived modern denudation rates are lower than long-term exhumation rates, likely because of rapid exhumation and removal of poorly consolidated sediments at the beginning of the range growth. On average, within the Kyrgyz data set, the highest ^{10}Be-derived denudation rates are recorded in the Terskey range, south of lake Issyk-Kul. Here, ^{10}Be-derived modern denudation rates are higher than ^{10}Be-derived paleo-denudation rates obtained from material dated to 2.0–2.7 Ma, which are comparable in magnitude to long-term exhumation rates inferred from AFT and AHe. The high ^{10}Be-derived denudation rates on the southern side of the Issyk-Kul basin compared to other sampled regions in the Kyrgyz Tian Shan suggest a recent increase in denudation rates on the northern slope of the Terskey range due to high glacial meltwater runoff, and/or admixing of previously shielded sediments with low ^{10}Be concentration.

We find that denudation in the Kyrgyz Tian Shan, particularly in the Terskey range, remained relatively steady during the Neogene and early Pleistocene despite the late Pliocene facies change from fine-grained sediment to conglomerates. Denudation in the Terskey range increased in the Quaternary, but this occurred after the onset and intensification of the Northern Hemisphere glaciations at 2.7 Ma. This delay in the denudational response of the landscape could indicate that glacial erosion in arid regions is detectable using cosmogenic radionuclides only after substantial cooling and extensive growth of glaciers. We acknowledge, however, that our ^{10}Be-derived paleo-denudation rate data are limited in size and areal extent and so might not be representative of the entire Kyrgyz Tian Shan and that other parts of the orogen might exhibit different temporal patterns of denudational response to Quaternary climate changes.

Comparison of our ^{10}Be-derived modern denudation rates with published data from the western Tian Shan, Northern Pamir and eastern (Chinese) Tian Shan show a spatial trend of decreasing denudation rates from west to east (Figure 2). This suggests that denudation in the Pamir and western Tian Shan is controlled by deformation caused by the northward motion of the Pamir, as well as high precipitation rates due to an orographic barrier to the westerlies created by the Pamir and Tian Shan. Further east, precipitation and tectonically driven denudation decrease and the denudational response of the landscape to Quaternary glaciations becomes detectable (Figure 7).

When considering the entire ^{10}Be data set, our analyses reveal weak but statistically significant correlations between log-transformed ^{10}Be-derived modern denudation rates and climatic metrics (precipitation and AI), and moderate correlations with strain rate and topographic metrics (Figure 6). When analyzed separately, the three data sets (namely, northern Pamir and western Tian Shan, Kyrgyz Tian Shan, and eastern Tians Shan) exhibit stronger correlations with topographic metrics and weaker correlations with climatic metrics. At the local scale, the picture is more complicated: albeit a moderate correlation is observed between denudation rate and topographic metrics in most of the regions with enough data points to warrant an analysis, climatic metrics such as annual rainfall, the rainfall of the wettest month, and the AI are stronger predictors of ^{10}Be denudation rate in some regions including the Terskey range, south of lake Issyk-Kul. The above highlights the complex linkages among tectonics, climate, and surface processes that may lead to local variations in the dominant controls on denudation.

Data Availability Statement

All cosmogenic radionuclide and thermochronology data included in this study are available as part of the Supporting Information and have been archived in the Zenodo open repository and can be accessed here: https://doi.org/10.5281/zenodo.8321776. Furthermore, all cosmogenic ^{10}Be-derived modern denudation rates will be made available in the OCTOPUS database (Codilean et al., 2018, 2022). The database can be accessed at https://octopusdata.org/ and is listed in the Registry of Research Data Repositories (https://www.re3data.org/) and follows FAIR data principles.

Acknowledgments
Funding was provided by the Deutsche Forschungs Gesellschaft e.V. (DFG) Grant SO 436/9-1 to E. Sobel, as well as by the German Federal Ministry of Education and Research (project TIPTIMON; support code 03G0809) and Volkswagen Foundation (Grant AZ 754 86860) to A. Landgraf and O. Korup. A. Kudriavtseva was also funded by the University of Wollongong (UOW) Faculty of Science, Medicine and Health and the UOW University Postgraduate Award fund. We are grateful to Marat Sheraliev, Alexander Mikolaichuk, Magda Patyniak, Christoph Grützner, Christian Haberland, and Sultan Baikulov for their help with sampling and logistics during field work in Kyrgyzstan. We thank Martin Struck for sample preparation work and Henry Munack for assistance with R. We acknowledge support from the Center for Accelerator Science at the Australian Nuclear Science and Technology Organisation (ANSTO) through the National Collaborative Research Infrastructure Strategy (NCRIS). Parts of this research were carried out at the Ion Beam Centre (IBC) at the Helmholtz-Zentrum Dresden-Rossendorf e.V., a member of the Helmholtz Association. We thank the DREAMS team, especially Stefan Pavetich, for assistance with AMS-measurements. Open Access funding enabled and organized by Projekt DEAL.

References

Abdrakhmatov, K., Aldazhanov, S., Hager, B., Hamburger, M. W., Herring, T. A., Kalabaev, K. B., et al. (1996). Relatively recent construction of the Tien Shan inferred from GPS measurements of present-day crustal deformation rates. *Nature*, *384*(6608), 450–453. https://doi.org/10.1038/384450a0

Abdrakhmatov, K., Weldon, R., Thompson, S. C., Burbank, D. W., Rubin, C., Miller, M., & Molnar, P. (2001). Onset, style and current rate of shortening in the central Tien Shan, Kyrgyz Republic. *Russian Geology and Geophysics*, *42*(10), 1585–1609.

Abdulhameed, S., Ratschbacher, L., Jonckheere, R., Gągała, Ł., Enkelmann, E., Käßner, A., et al. (2020). Tajik basin and southwestern Tian Shan, northwestern India-Asia collision zone: 2. Timing of basin inversion, Tian Shan mountain building, and relation to Pamir-plateau advance and deep India-Asia indentation. *Tectonics*, *39*(5), e2019TC005873. https://doi.org/10.1029/2019TC005873

Aizen, E. M., Aizen, V. B., Melack, J. M., Nakamura, T., & Ohta, T. (2001). Precipitation and atmospheric circulation patterns at mid-latitudes of Asia. *International Journal of Climatology: A Journal of the Royal Meteorological Society*, *21*(5), 535–556. https://doi.org/10.1002/joc.626

Aizen, V. B., Aizen, E. M., Joswiak, D. R., Fujita, K., Takeuchi, N., & Nikitin, S. A. (2006). Climatic and atmospheric circulation pattern variability from ice-core isotope/geochemistry records (Altai, Tien Shan and Tibet). *Annals of Glaciology*, *43*, 49–60. https://doi.org/10.3189/172756406781812078

Aizen, V. B., Aizen, E. M., Melack, J. M., & Dozier, J. (1997). Climatic and hydrologic changes in the Tien Shan, Central Asia. *Journal of Climate*, *10*(6), 1393–1404. https://doi.org/10.1175/1520-0442(1997)010<1393:CAHCIT>2.0.CO;2

Alexeiev, D. V., Bykadorov, V. A., Volozh, Y. A., & Sapozhnikov, R. B. (2017). Kinematic analysis of Jurassic grabens of southern Turgai and the role of the Mesozoic stage in the evolution of the Karatau–Talas–Ferghana strike-slip fault, southern Kazakhstan and Tian Shan. *Geotectonics*, *51*(2), 105–120. https://doi.org/10.1134/S0016852117020029

Amidon, W. H., & Hynek, S. A. (2010). Exhumational history of the north central Pamir. *Tectonics*, *29*(5), TC5017. https://doi.org/10.1029/2009TC002589

Avouac, J. P., & Burov, E. B. (1996). Erosion as a driving mechanism of intracontinental mountain growth. *Journal of Geophysical Research*, *101*(B8), 17747–17769. https://doi.org/10.1029/96JB01344

Bakirov, A. B., & Maksumova, R. A. (2001). Geodynamic evolution of the Tien Shan lithosphere. *Russian Geology and Geophysics*, *42*(10), 1435–1443.

Baldwin, J., & Vecchi, G. (2016). Influence of the Tian Shan on arid extratropical Asia. *Journal of Climate*, *29*(16), 5741–5762. https://doi.org/10.1175/JCLI-D-15-0490.1

Bande, A., Sobel, E. R., Mikolaichuk, A., Schmidt, A., & Stockli, D. F. (2017). Exhumation history of the western Kyrgyz Tien Shan: Implications for intramontane basin formation. *Tectonics*, *36*(1), 163–180. https://doi.org/10.1002/2016TC004284

Bande, A., Sobel, E. R., Mikolaichuk, A., & Torres Acosta, V. (2017). Talas–Fergana Fault Cenozoic timing of deformation and its relation to Pamir indentation. *Geological Society, London, Special Publications*, *427*(1), 295–311. https://doi.org/10.1144/SP427.1

Batbaatar, J., Gillespie, A. R., Koppes, M., Clark, D. H., Chadwick, O. A., Fink, D., et al. (2021). Glacier development in continental climate regions of Central Asia. In R. B. Waitt, G. D. Thackray, & A. R. Gillespie (Eds.), *Untangling the quaternary period—A legacy of Stephen C. Porter. Geological Society of America, special paper* (Vol. 548, pp. 119–149). https://doi.org/10.1130/2020.2548(07

Bazhenov, M. L., Collins, A. Q., Degtyarev, K. E., Levashova, N. M., Mikolaichuk, A. V., Pavlov, V. E., & Van der Voo, R. (2003). Paleozoic northward drift of the North Tien Shan (Central Asia) as revealed by Ordovician and Carboniferous palaeomagnetism. *Tectonophysics*, *366*(1–2), 113–141. https://doi.org/10.1016/S0040-1951(03)00075-1

Bazhenov, M. L., & Mikolaichuk, A. V. (2004). Structural evolution of Central Asia to the North of Tibet: A synthesis of paleomagnetic and geological data. *Geotectonics*, *38*(5), 379–393.

Bernard, T., & Sinclair, H. D. (2022). Accelerated sediment delivery to continental margins during post-orogenic rebound of mountain ranges. *Basin Research*, *00*(2), 1–20. https://doi.org/10.1111/bre.12727

Bershaw, J., & Lechler, A. R. (2019). The isotopic composition of meteoric water along altitudinal transects in the Tian Shan of Central Asia. *Chemical Geology*, *516*, 68–78. https://doi.org/10.1016/j.chemgeo.2019.03.032

Biske, Y. S., & Seltmann, R. (2010). Paleozoic Tian-Shan as a transitional region between the Rheic and Urals-Turkestan oceans. *Gondwana Research*, *17*(2–3), 602–613. https://doi.org/10.1016/j.gr.2009.11.014

Blomdin, R., Stroeven, A. P., Harbor, J. M., Lifton, N. A., Heyman, J., Gribenski, N., et al. (2016). Evaluating the timing of former glacier expansions in the Tian Shan: A key step towards robust spatial correlations. *Quaternary Science Reviews*, *153*, 78–96. https://doi.org/10.1016/j.quascirev.2016.07.029

Botsyun, S., Mutz, S. G., Ehlers, T. A., Koptev, A., Wang, X., Schmidt, B., et al. (2022). Influence of large-scale atmospheric dynamics on precipitation seasonality of the Tibetan plateau and Central Asia in cold and warm climates during the late Cenozoic. *Journal of Geophysical Research: Atmospheres*, *127*(12), e2021JD035810. https://doi.org/10.1029/2021JD035810

Braucher, R., Merchel, S., Borgomano, J., & Bourlès, D. (2011). Production of cosmogenic radionuclides at great depth: A multi element approach. *Earth and Planetary Science Letters*, *309*(1–2), 1–9. https://doi.org/10.1016/j.epsl.2011.06.036

Bullen, M. E., Burbank, D. W., & Garver, J. I. (2003). Building the northern Tien Shan: Integrated thermal, structural, and topographic constraints. *The Journal of Geology*, *111*(2), 149–165. https://doi.org/10.1086/345840

Bullen, M. E., Burbank, D. W., Garver, J. I., & Abdrakhmatov, K. Y. (2001). Late Cenozoic tectonic evolution of the northwestern Tien Shan: New age estimates for the initiation of mountain building. *Geological Society of America Bulletin*, *113*(12), 1544–1559. https://doi.org/10.1130/0016-7606(2001)113<1544:LCTEOT>2.0.CO;2

Burbank, D. W., Blythe, A. E., Putkonen, J., Pratt-Sitaula, B., Gabet, E., Oskin, M., et al. (2003). Decoupling of erosion and precipitation in the Himalayas. *Nature*, *426*(6967), 652–655. https://doi.org/10.1038/nature02187

Burtman, V. S., & Molnar, P. (1993). Geological and geophysical evidence for deep subduction of continental crust beneath the Pamir. In *Special paper GSA 281*. https://doi.org/10.1130/SPE281-p1

Carrapa, B., Mustapha, F. S., Cosca, M., Gehrels, G., Schoenbohm, L. M., Sobel, E. R., et al. (2014). Multisystem dating of modern river detritus from Tajikistan and China: Implications for crustal evolution and exhumation of the Pamir. *Lithosphere*, *6*(6), 443–455. https://doi.org/10.1130/L360.1

Caves, J. K., Moragne, D. Y., Ibarra, D. E., Bayshashov, B. U., Gao, Y., Jones, M. M., et al. (2016). The Neogene de-greening of Central Asia. *Geology*, *44*(11), 887–890. https://doi.org/10.1130/G38267.1

Caves, J. K., Winnick, M. J., Graham, S. A., Sjostrom, D. J., Mulch, A., & Chamberlain, C. P. (2015). Role of the westerlies in Central Asia climate over the Cenozoic. *Earth and Planetary Science Letters*, *428*, 33–43. https://doi.org/10.1016/j.epsl.2015.07.023

Caves Rugenstein, J. K., & Chamberlain, C. P. (2018). The evolution of hydroclimate in Asia over the Cenozoic: A stable-isotope perspective. *Earth-Science Reviews*, *185*, 1129–1156. https://doi.org/10.1016/j.earscirev.2018.09.003

Charreau, J., Blard, P. H., Lavé, J., Dominguez, S., & Li, W. S. (2023). Unsteady topography in the eastern Tianshan due to imbalance between denudation and crustal thickening. *Tectonophysics*, *848*, 1–16. https://doi.org/10.1016/j.tecto.2022.229702
Charreau, J., Blard, P. H., Puchol, N., Avouac, J. P., Lallier-Vergès, E., Bourlès, D., et al. (2011). Paleo-erosion rates in Central Asia since 9 Ma: A transient increase at the onset of quaternary glaciations? *Earth and Planetary Science Letters*, *304*(1–2), 85–92. https://doi.org/10.1016/j.epsl.2011.01.018
Charreau, J., Gumiaux, C., Avouac, J. P., Augier, R., Chen, Y., Barrier, L., et al. (2009). The Neogene Xiyu Formation, a diachronous prograding gravel wedge at front of the Tianshan: Climatic and tectonic implications. *Earth and Planetary Science Letters*, *287*(3–4), 298–310. https://doi.org/10.1016/j.epsl.2009.07.035
Charreau, J., Saint-Carlier, D., Dominguez, S., Lavé, J., Blard, P. H., Avouac, J. P., et al. (2017). Denudation outpaced by crustal thickening in the eastern Tianshan. *Earth and Planetary Science Letters*, *479*, 179–191. https://doi.org/10.1016/j.epsl.2017.09.025
Chen, J., Burbank, D. W., Scharer, K. M., Sobel, E., Yin, J., Rubin, C., & Zhao, R. (2002). Magnetochronology of the upper Cenozoic strata in the southwestern Chinese Tian Shan: Rates of Pleistocene folding and thrusting. *Earth and Planetary Science Letters*, *195*(1–2), 113–130. https://doi.org/10.1016/S0012-821X(01)00579-9
Chen, S. A., Michaelides, K., Richards, D. A., & Singer, M. B. (2022). Exploring exogenous controls on short-versus long-term erosion rates globally. *Earth Surface Dynamics*, *10*(6), 1055–1078. https://doi.org/10.5194/esurf-10-1055-2022
Codilean, A. T. (2006). Calculation of the cosmogenic nuclide production topographic shielding scaling factor for large areas using DEMs. *Earth Surface Processes and Landforms*, *31*(6), 785–794. https://doi.org/10.1002/esp.1336
Codilean, A. T., Fülöp, R.-H., Wilcken, K. M., Koutamanis, D. S., Fink, D., Fifield, L. K., et al. (2023). Cosmogenic Be-10 and Al-26 sample preparation at the University of Wollongong. *Nuclear Instruments and Methods in Physics Research Section B: Beam Interactions with Materials and Atoms*, *535*, 61–73. https://doi.org/10.1016/j.nimb.2022.12.003
Codilean, A. T., Munack, H., Cohen, T. J., Saktura, W. M., Gray, A., & Mudd, S. M. (2018). OCTOPUS: An open cosmogenic isotope and luminescence database. *Earth System Science Data*, *10*(4), 2123–2139. https://doi.org/10.5194/essd-10-2123-2018
Codilean, A. T., Munack, H., Saktura, W. M., Cohen, T. J., Jacobs, Z., Ulm, S., et al. (2022). OCTOPUS database (v.2). *Earth System Science Data*, *14*(8), 3695–3713. https://doi.org/10.5194/essd-14-3695-2022
Compo, G. P., Whitaker, J. S., Sardeshmukh, P. D., Matsui, N., Allan, R. J., Yin, X., et al. (2011). The Twentieth century reanalysis project. *Quarterly Journal of the Royal Meteorological Society*, *137*(654), 1–28. https://doi.org/10.1002/qj.776
De Grave, J. (2003). *Apatite fission-track thermochronology of the Altai Mountains (South Siberia, Russia) and the Tien Shan Mountains (Kyrgyzstan): Relevance to Meso-Cenozoic tectonics and denudation in Central Asia* (Doctoral dissertation). Ghent University.
De Grave, J., Glorie, S., Buslov, M. M., Stockli, D. F., McWilliams, M. O., Batalev, V. Y., & Van den haute, P. (2013). Thermo-tectonic history of the Issyk-Kul basement (Kyrgyz northern Tien Shan, Central Asia). *Gondwana Research*, *23*(3), 998–1020. https://doi.org/10.1016/j.gr.2012.06.014
DiBiase, R. A. (2018). Short communication: Increasing vertical attenuation length of cosmogenic nuclide production on steep slopes negates topographic shielding corrections for catchment erosion rates. *Earth Surface Dynamics*, *6*(4), 923–931. https://doi.org/10.5194/esurf-6-923-2018
Dosseto, A., & Schaller, M. (2016). The erosion response to Quaternary climate change quantified using uranium isotopes and in situ-produced cosmogenic nuclides. *Earth-Science Reviews*, *155*, 60–81. https://doi.org/10.1016/j.earscirev.2016.01.015
Farley, K. A. (2000). Helium diffusion from apatite: General behavior as illustrated by Durango fluorapatite. Journal of Geophysical Research. *Solid Earth*, *105*(B2), 2903–2914. https://doi.org/10.1029/1999JB900348
Farr, T. G., Rosen, P. A., Caro, E., Crippen, R., Duren, R., Hensley, S., et al. (2007). The Shuttle radar Topography Mission. *Reviews of Geophysics*, *45*(2), RG2004. https://doi.org/10.1029/2005RG000183
Fick, S. E., & Hijmans, R. J. (2017). WorldClim 2: New 1-km spatial resolution climate surfaces for global land areas. *International Journal of Climatology*, *37*(12), 4302–4315. https://doi.org/10.1002/joc.5086
Fink, D., & Smith, A. (2007). An inter-comparison of ^{10}Be and ^{26}Al AMS reference standards and the ^{10}Be half-life. *Nuclear Instruments and Methods in Physics Research Section B: Beam Interactions with Materials and Atoms*, *259*(1), 600–609. https://doi.org/10.1016/j.nimb.2007.01.299
Forte, A. M., & Whipple, K. X. (2019). The topographic analysis kit (TAK) for TopoToolbox. *Earth Surface Dynamics*, *7*(1), 87–95. https://doi.org/10.5194/esurf-7-87-2019
Fuchs, M. C., Gloaguen, R., Merchel, S., Pohl, E., Sulaymonova, V. A., Andermann, C., & Rugel, G. (2015). Denudation rates across the Pamir based on ^{10}Be concentrations in fluvial sediments: Dominance of topographic over climatic factors. *Earth Surface Dynamics*, *3*(3), 423–439. https://doi.org/10.5194/esurf-3-423-2015
Ganti, V., Von Hagke, C., Scherler, D., Lamb, M. P., Fischer, W. W., & Avouac, J. P. (2016). Time scale bias in erosion rates of glaciated landscapes. *Science Advances*, *2*(10), e1600204. https://doi.org/10.1126/sciadv.1600204
Glorie, S., & De Grave, J. (2016). Exhuming the Meso–Cenozoic Kyrgyz Tianshan and Siberian Altai-Sayan: A review based on low-temperature thermochronology. *Geoscience Frontiers*, *7*(2), 155–170. https://doi.org/10.1016/j.gsf.2015.04.003
Glorie, S., De Grave, J., Buslov, M. M., Elburg, M. A., Stockli, D. F., Gerdes, A., & Van den haute, P. (2010). Multi-method chronometric constraints on the evolution of the northern Kyrgyz Tien Shan granitoids (Central Asian Orogenic belt): From emplacement to exhumation. *Journal of Asian Earth Sciences*, *38*(3–4), 131–146. https://doi.org/10.1016/j.jseaes.2009.12.009
Glorie, S., De Grave, J., Buslov, M. M., Zhimulev, F. I., Stockli, D. F., Batalev, V. Y., et al. (2011). Tectonic history of the Kyrgyz South Tien Shan (Atbashi-Inylchek) suture zone: The role of inherited structures during deformation-propagation. *Tectonics*, *30*(6), TC6016. https://doi.org/10.1029/2011TC002949
Goode, J. K., Burbank, D. W., & Ormukov, C. (2014). Pliocene-Pleistocene initiation, style, and sequencing of deformation in the central Tien Shan. *Tectonics*, *33*(4), 464–484. https://doi.org/10.1002/2013TC003394
Granger, D. E., & Schaller, M. (2014). Cosmogenic nuclides and erosion at the watershed scale. *Elements*, *10*(5), 369–373. https://doi.org/10.2113/gselements.10.5.369
Grin, E., Schaller, M., & Ehlers, T. A. (2018). Spatial distribution of cosmogenic ^{10}Be derived denudation rates between the Western Tian Shan and Northern Pamir, Tajikistan. *Geomorphology*, *321*, 1–15. https://doi.org/10.1016/j.geomorph.2018.08.007
Guan, X., Ma, Y., Lu, H., Jiang, Y., Pang, L., Zheng, X., & Li, Y. (2022). Topographic and climatic controls on decadal-scale catchment-basin erosion rates in the northern Chinese Tian Shan. *Catena*, *210*, 105862. https://doi.org/10.1016/j.catena.2021.105862
Guerit, L., Barrier, L., Jolivet, M., Fu, B., & Métivier, F. (2016). Denudation intensity and control in the Chinese Tian Shan: New constraints from mass balance on catchment-alluvial fan systems. *Earth Surface Processes and Landforms*, *41*(8), 1088–1106. https://doi.org/10.1002/esp.3890
Hartmann, J., & Moosdorf, N. (2012). The new global lithological map database GLiM: A representation of rock properties at the Earth surface. *Geochemistry, Geophysics, Geosystems*, *13*(12), Q12004. https://doi.org/10.1029/2012gc004370

Hayashi, T., Yamanaka, T., Hikasa, Y., Sato, M., Kuwahara, Y., & Ohno, M. (2020). Latest Pliocene Northern Hemisphere glaciation amplified by intensified Atlantic meridional overturning circulation. *Communications Earth & Environment*, *1*(1), 25. https://doi.org/10.1038/s43247-020-00023-4

Hecht, H., & Oguchi, T. (2017). Global evaluation of erosion rates in relation to tectonics. *Progress in Earth and Planetary Science*, *4*(1), 1–9. https://doi.org/10.1186/s40645-017-0156-3

Heermance, R. V., Chen, J., Burbank, D. W., & Wang, C. (2007). Chronology and tectonic controls of Late Tertiary deposition in the southwestern Tian Shan foreland, NW China. *Basin Research*, *19*(4), 599–632. https://doi.org/10.1111/j.1365-2117.2007.00339.x

Hendrix, M. S., Graham, S. A., Carroll, A. R., Sobel, E. R., McKnight, C. L., Schulein, B. J., & Wang, Z. (1992). Sedimentary record and climatic implications of recurrent deformation in the Tian Shan: Evidence from Mesozoic strata of the north Tarim, south Junggar, and Turpan basins, northwest China. *Geological Society of America Bulletin*, *104*(1), 53–79. https://doi.org/10.1130/0016-7606(1992)104<0053:SRACIO>2.3.CO;2

Herman, F., Braun, J., Deal, E., & Prasicek, G. (2018). The response time of glacial erosion. *Journal of Geophysical Research: Earth Surface*, *123*(4), 801–817. https://doi.org/10.1002/2017JF004586

Herman, F., & Champagnac, J. D. (2016). Plio-Pleistocene increase of erosion rates in mountain belts in response to climate change. *Terra Nova*, *28*(1), 2–10. https://doi.org/10.1111/ter.12186

Horn, B. K. P. (1981). Hill shading and the reflectance map. *Proceedings of the IEEE*, *69*(1), 14–47. https://doi.org/10.1109/PROC.1981.11918

Ischuk, A., Bendick, R., Rybin, A., Molnar, P., Khan, S. F., Kuzikov, S., et al. (2013). Kinematics of the Pamir and Hindu Kush regions from GPS geodesy. *Journal of Geophysical Research: Solid Earth*, *118*(5), 2408–2416. https://doi.org/10.1002/jgrb.50185

Jepson, G., Carrapa, B., Gillespie, J., Feng, R., DeCelles, P. G., Kapp, P., et al. (2021). Climate as the great equalizer of continental-scale erosion. *Geophysical Research Letters*, *48*(20), e2021GL095008. https://doi.org/10.1029/2021GL095008

Jolivet, M., Dominguez, S., Charreau, J., Chen, Y., Li, Y., & Wang, Q. (2010). Mesozoic and Cenozoic tectonic history of the central Chinese Tian Shan: Reactivated tectonic structures and active deformation. *Tectonics*, *29*(6), 1–30. https://doi.org/10.1029/2010TC002712

Kent-Corson, M. L., Ritts, B. D., Zhuang, G., Bovet, P. M., Graham, S. A., & Chamberlain, C. P. (2009). Stable isotopic constraints on the tectonic, topographic, and climatic evolution of the northern margin of the Tibetan Plateau. *Earth and Planetary Science Letters*, *282*(1–4), 158–166. https://doi.org/10.1016/j.epsl.2009.03.011

Kohl, C. P., & Nishiizumi, K. (1992). Chemical isolation of quartz for measurement of in-situ-produced cosmogenic nuclides. *Geochimica et Cosmochimica Acta*, *56*(9), 3583–3587. https://doi.org/10.1016/0016-7037(92)90401-4

Koppes, M. N., Gillespie, A. R., Burke, R. M., Thompson, S. C., & Stone, J. (2008). Late Quaternary glaciation in the Kyrgyz Tien Shan. *Quaternary Science Reviews*, *27*(7–8), 846–866. https://doi.org/10.1016/j.quascirev.2008.01.009

Koppes, M. N., & Montgomery, D. R. (2009). The relative efficacy of fluvial and glacial erosion over modern to orogenic timescales. *Nature Geoscience*, *2*(9), 644–647. https://doi.org/10.1038/ngeo616

Kreemer, C., Blewitt, G., & Klein, E. C. (2014). A geodetic plate motion and global strain rate model. *Geochemistry, Geophysics, Geosystems*, *15*(10), 3849–3889. https://doi.org/10.1002/2014gc005407

Kudriavtseva, A., Sobel, E. R., Codilean, A. T., Meijers, M. J. M., Mulch, A., Hoke, G. D., et al. (2023). Neogene aridification and lake development in the Issyk-Kul basin, Kyrgyzstan. *Basin Research*, *00*(3), 1–35. https://doi.org/10.1111/bre.12751

Kufner, S. K., Schurr, B., Sippl, C., Yuan, X., Ratschbacher, L., Ischuk, A., et al. (2016). Deep India meets deep Asia: Lithospheric indentation, delamination and break-off under Pamir and Hindu Kush (Central Asia). *Earth and Planetary Science Letters*, *435*, 171–184. https://doi.org/10.1016/j.epsl.2015.11.046

Kutuzov, S., & Shahgedanova, M. (2009). Glacier retreat and climatic variability in the eastern Terskey–Alatoo, inner Tien Shan between the middle of the 19th century and beginning of the 21st century. *Global and Planetary Change*, *69*(1–2), 59–70. https://doi.org/10.1016/j.gloplacha.2009.07.001

Landgraf, A., Dzhumabaeva, A., Abdrakhmatov, K. E., Strecker, M. R., Macaulay, E. A., Arrowsmith, J. R., et al. (2016). Repeated large-magnitude earthquakes in a tectonically active, low-strain continental interior: The northern Tien Shan, Kyrgyzstan. *Journal of Geophysical Research: Solid Earth*, *121*(5), 3888–3910. https://doi.org/10.1002/2015JB012714

Lauterbach, S., Witt, R., Plessen, B., Dulski, P., Prasad, S., Mingram, J., et al. (2014). Climatic imprint of the mid-latitude Westerlies in the Central Tian Shan of Kyrgyzstan and teleconnections to North Atlantic climate variability during the last 6000 years. *The Holocene*, *24*(8), 970–984. https://doi.org/10.1177/0959683614534741

Li, H.-D., Zhou, J.-B., & Wilde, S. A. (2022). Nature and development of the South Tianshan-Solonker suture zone. *Earth-Science Reviews*, *233*, 104189. https://doi.org/10.1016/j.earscirev.2022.104189

Li, Q., Yang, T., Zhang, F., Qi, Z., & Li, L. (2019). Snow depth reconstruction over last century: Trend and distribution in the Tianshan Mountains, China. *Global and Planetary Change*, *173*, 73–82. https://doi.org/10.1016/j.gloplacha.2018.12.008

Li, W., Chen, Y., Yuan, X., Xiao, W., & Windley, B. F. (2022). Intracontinental deformation of the Tianshan Orogen in response to India-Asia collision. *Nature Communications*, *13*(1), 3738. https://doi.org/10.1038/s41467-022-30795-6

Li, Y. P., Robinson, A. C., Gadoev, M., & Oimuhammadzoda, I. (2020). Was the Pamir salient built along a Late Paleozoic embayment on the southern Asian margin? *Earth and Planetary Science Letters*, *550*, 116554. https://doi.org/10.1016/j.epsl.2020.116554

Lisiecki, L. E., & Raymo, M. E. (2005). A Pliocene-Pleistocene stack of 57 globally distributed benthic $\delta^{18}O$ records. *Paleoceanography*, *20*(1), PA1003. https://doi.org/10.1029/2004PA001071

Liu, Y., Métivier, F., Gaillardet, J., Ye, B., Meunier, P., Narteau, C., et al. (2011). Erosion rates deduced from seasonal mass balance along the upper Urumqi River in Tianshan. *Solid Earth*, *2*(2), 283–301. https://doi.org/10.5194/se-2-283-2011

Macaulay, E. A., Sobel, E. R., Mikolaichuk, A., Kohn, B., & Stuart, F. M. (2014). Cenozoic deformation and exhumation history of the Central Kyrgyz Tien Shan. *Tectonics*, *33*(2), 135–165. https://doi.org/10.1002/2013TC003376

Macaulay, E. A., Sobel, E. R., Mikolaichuk, A., Landgraf, A., Kohn, B., & Stuart, F. (2013). Thermochronologic insight into late Cenozoic deformation in the basement-cored Terskey Range, Kyrgyz Tien Shan. *Tectonics*, *32*(3), 487–500. https://doi.org/10.1002/tect.20040

Mariotti, A., Blard, P. H., Charreau, J., Toucanne, S., Jorry, S. J., Molliex, S., et al. (2021). Nonlinear forcing of climate on mountain denudation during glaciations. *Nature Geoscience*, *14*(1), 16–22. https://doi.org/10.1038/s41561-020-00672-2

Miao, Y., Herrmann, M., Wu, F., Yan, X., & Yang, S. (2012). What controlled mid–late Miocene long-term aridification in Central Asia?—Global cooling or Tibetan plateau uplift: A review. *Earth-Science Reviews*, *112*(3–4), 155–172. https://doi.org/10.1016/j.earscirev.2012.02.003

Molnar, P. (2004). Late Cenozoic increase in accumulation rates of terrestrial sediment: How might climate change have affected erosion rates? *Annual Review of Earth and Planetary Sciences*, *32*(1), 67–89. https://doi.org/10.1146/annurev.earth.32.091003.143456

Molnar, P., & England, P. (1990). Late Cenozoic uplift of mountain ranges and global climate change: Chicken or egg? *Nature*, *346*(6279), 29–34. https://doi.org/10.1038/346029a0

Molnar, P., & Tapponnier, P. (1975). Cenozoic Tectonics of Asia: Effects of a Continental Collision: Features of recent continental tectonics in Asia can be interpreted as results of the India-Eurasia collision. *Science*, *189*(4201), 419–426. https://doi.org/10.1126/science.189.4201.419

Montgomery, D. R., & Brandon, M. T. (2002). Topographic controls on erosion rates in tectonically active mountain ranges. *Earth and Planetary Science Letters*, *201*(3–4), 481–489. https://doi.org/10.1016/S0012-821X(02)00725-2

Mudd, S. M., Harel, M. A., Hurst, M. D., Grieve, S. W., & Marrero, S. M. (2016). The CAIRN method: Automated, reproducible calculation of catchment-averaged denudation rates from cosmogenic nuclide concentrations. *Earth Surface Dynamics*, *4*(3), 655–674. https://doi.org/10.5194/esurf-4-655-2016

Nishiizumi, K., Imamura, M., Caffee, M. W., Southon, J. R., Finkel, R. C., & McAninch, J. (2007). Absolute calibration of ^{10}Be AMS standards. *Nuclear Instruments and Methods in Physics Research Section B: Beam Interactions with Materials and Atoms*, *258*(2), 403–413. https://doi.org/10.1016/j.nimb.2007.01.297

Norton, K. P., & Schlunegger, F. (2017). Lack of a weathering signal with increased Cenozoic erosion? *Terra Nova*, *29*(5), 265–272. https://doi.org/10.1111/ter.12278

Portenga, E. W., & Bierman, P. R. (2011). Understanding Earth's eroding surface with 10Be. *Geological Society of America Today*, *21*(8), 4–10. https://doi.org/10.1130/G111A.1

Puchol, N., Charreau, J., Blard, P. H., Lavé, J., Dominguez, S., Pik, R., et al. (2017). Limited impact of Quaternary glaciations on denudation rates in Central Asia. *GSA Bulletin*, *129*(3–4), 479–499. https://doi.org/10.1130/B31475.1

Ramstein, G., Fluteau, F., Besse, J., & Joussaume, S. (1997). Effect of orogeny, plate motion and land–sea distribution on Eurasian climate change over the past 30 million years. *Nature*, *386*(6627), 788–795. https://doi.org/10.1038/386788a0

Raup, B., Racoviteanu, A., Khalsa, S. J. S., Helm, C., Armstrong, R., & Arnaud, Y. (2007). The GLIMS geospatial glacier database: A new tool for studying glacier change. *Global and Planetary Change*, *56*(1–2), 101–110. https://doi.org/10.1016/j.gloplacha.2006.07.018

Raymo, M. E., & Ruddiman, W. F. (1992). Tectonic forcing of late Cenozoic climate. *Nature*, *359*(6391), 117–122. https://doi.org/10.1038/359117a0

Reiners, P. W., & Brandon, M. T. (2006). Using thermochronology to understand orogenic erosion. *Annual Review of Earth and Planetary Sciences*, *34*(1), 419–466. https://doi.org/10.1146/annurev.earth.34.031405.125202

Richter, F., Pearson, J., Vilkas, M., Heermance, R. V., Garzione, C. N., Cecil, M. R., et al. (2022). Growth of the southern Tian Shan-Pamir and its impact on central Asian climate. *GSA Bulletin*. https://doi.org/10.1130/B36471.1

Ricketts, R. D., Johnson, T. C., Brown, E. T., Rasmussen, K. A., & Romanovsky, V. V. (2001). The Holocene paleolimnology of Lake Issyk-Kul, Kyrgyzstan: Trace element and stable isotope composition of ostracodes. *Palaeogeography, Palaeoclimatology, Palaeoecology*, *176*(1–4), 207–227. https://doi.org/10.1016/S0031-0182(01)00339-X

Rugel, G., Pavetich, S., Akhmadaliev, S., Baez, S. M. E., Scharf, A., Ziegenrücker, R., & Merchel, S. (2016). The first four years of the AMS-facility DREAMS: Status and developments for more accurate radionuclide data. *Nuclear Instruments and Methods in Physics Research Section B: Beam Interactions with Materials and Atoms*, *370*, 94–100. https://doi.org/10.1016/j.nimb.2016.01.012

Ruggieri, E., Herbert, T., Lawrence, K. T., & Lawrence, C. E. (2009). Change point method for detecting regime shifts in paleoclimatic time series: Application to δ^{18}O time series of the Plio-Pleistocene. *Paleoceanography*, *24*(1), PA1204. https://doi.org/10.1029/2007PA001568

Rutte, D., Ratschbacher, L., Khan, J., Stübner, K., Hacker, B. R., Stearns, M. A., et al. (2017). Building the Pamir-Tibetan Plateau—Crustal stacking, extensional collapse, and lateral extrusion in the central Pamir: 2. Timing and rates. *Tectonics*, *36*(3), 385–419. https://doi.org/10.1002/2016TC004294

Sanhueza-Pino, K., Korup, O., Hetzel, R., Munack, H., Weidinger, J. T., Dunning, S., et al. (2011). Glacial advances constrained by ^{10}Be exposure dating of bedrock landslides, Kyrgyz Tien Shan. *Quaternary Research*, *76*(3), 295–304. https://doi.org/10.1016/j.yqres.2011.06.013

Schaefer, J. M., Codilean, A. T., Willenbring, J. K., Lu, Z.-T., Keisling, B., Fülöp, R.-H., & Val, P. (2022). Cosmogenic nuclide techniques. *Nature Reviews Methods Primers*, *2*(1), 18. https://doi.org/10.1038/s43586-022-00096-9

Schildgen, T. F., van der Beek, P. A., Sinclair, H. D., & Thiede, R. C. (2018). Spatial correlation bias in late-Cenozoic erosion histories derived from thermochronology. *Nature*, *559*(7712), 89–93. https://doi.org/10.1038/s41586-018-0260-6

Schwanghart, W., & Kuhn, N. J. (2010). TopoToolbox: A set of Matlab functions for topographic analysis. *Environmental Modelling & Software*, *25*(6), 770–781. https://doi.org/10.1016/j.envsoft.2009.12.002

Schwanghart, W., & Scherler, D. (2014). TopoToolbox 2—MATLAB-based software for topographic analysis and modeling in Earth surface sciences. *Earth Surface Dynamics*, *2*(1), 1–7. https://doi.org/10.5194/esurf-2-1-2014

Schwarz, A., Turner, F., Lauterbach, S., Plessen, B., Krahn, K. J., Glodniok, S., et al. (2017). Mid-to late Holocene climate-driven regime shifts inferred from diatom, ostracod and stable isotope records from Lake Son Kol (Central Tian Shan, Kyrgyzstan). *Quaternary Science Reviews*, *177*, 340–356. https://doi.org/10.1016/j.quascirev.2017.10.009

Shen, Y. J., Shen, Y., Goetz, J., & Brenning, A. (2016). Spatial-temporal variation of near-surface temperature lapse rates over the Tianshan Mountains, Central Asia. *Journal of Geophysical Research: Atmospheres*, *121*(23), 14-006. https://doi.org/10.1002/2016JD025711

Shuster, D. L., Cuffey, K. M., Sanders, J. W., & Balco, G. (2011). Thermochronometry reveals headward propagation of erosion in an alpine landscape. *Science*, *332*(6025), 84–88. https://doi.org/10.1126/science.1198401

Sippl, C., Ratschbacher, L., Schurr, B., Krumbiegel, C., Rui, H., Pingren, L., & Abdybachaev, U. (2014). The 2008 Nura earthquake sequence at the Pamir-Tian Shan collision zone, southern Kyrgyzstan. *Tectonics*, *33*(12), 2382–2399. https://doi.org/10.1002/2014TC003705

Sobel, E. R., Chen, J., & Heermance, R. V. (2006). Late Oligocene–early Miocene initiation of shortening in the southwestern Chinese Tian Shan: Implications for Neogene shortening rate variations. *Earth and Planetary Science Letters*, *247*(1–2), 70–81. https://doi.org/10.1016/j.epsl.2006.03.048

Sobel, E. R., Oskin, M., Burbank, D., & Mikolaichuk, A. (2006). Exhumation of basement-cored uplifts: Example of the Kyrgyz Range quantified with apatite fission track thermochronology. *Tectonics*, *25*(2), TC2008. https://doi.org/10.1029/2005TC001809

Sorg, A., Bolch, T., Stoffel, M., Solomina, O., & Beniston, M. (2012). Climate change impacts on glaciers and runoff in Tien Shan (Central Asia). *Nature Climate Change*, *2*(10), 725–731. https://doi.org/10.1038/nclimate1592

Stone, J. O. (2000). Air pressure and cosmogenic isotope production. *Journal of Geophysical Research*, *105*(B10), 23753–23759. https://doi.org/10.1029/2000JB900181

Stroeven, A. P., Hättestrand, C., Heyman, J., Kleman, J., & Morén, B. M. (2013). Glacial geomorphology of the Tian Shan. *Journal of Maps*, *9*(4), 505–512. https://doi.org/10.1080/17445647.2013.820879

Thompson, J., Burbank, D., Li, T., Chen, J., & Bookhagen, B. (2015). Late Miocene northward propagation of the northeast Pamir thrust system, northwest China. *Tectonics*, *34*(3), 510–534. https://doi.org/10.1002/2014TC003690

Thompson, S. C., Weldon, R. J., Rubin, C. M., Abdrakhmatov, K., Molnar, P., & Berger, G. W. (2002). Late Quaternary slip rates across the central Tien Shan, Kyrgyzstan, Central Asia. *Journal of Geophysical Research*, *107*(B9), ETG-7. https://doi.org/10.1029/2001JB000596

Unger-Shayesteh, K., Vorogushyn, S., Farinotti, D., Gafurov, A., Duethmann, D., Mandychev, A., & Merz, B. (2013). What do we know about past changes in the water cycle of Central Asian headwaters? A review. *Global and Planetary Change*, *110*, 4–25. https://doi.org/10.1016/j.gloplacha.2013.02.004

Van der Beek, P., & Schildgen, T. F. (2023). *age2exhume*—A MATLAB/Python script to calculate steady-state vertical exhumation rates from thermochronometric ages and application to the Himalaya. *Geochronology*, *5*(1), 35–49. https://doi.org/10.5194/gchron-5-35-2023

Wang, X., Carrapa, B., Sun, Y., Dettman, D. L., Chapman, J. B., Caves Rugenstein, J. K., et al. (2020). The role of the westerlies and orography in Asian hydroclimate since the late Oligocene. *Geology*, *48*(7), 728–732. https://doi.org/10.1130/G47400.1

Wang, Y., Zhang, J., Huang, X., & Wang, Z. (2023). Cenozoic exhumation of the Tianshan as constrained by regional low-temperature thermochronology. *Earth-Science Reviews*, *237*, 104325. https://doi.org/10.1016/j.earscirev.2023.104325

Westerhold, T., Marwan, N., Drury, A. J., Liebrand, D., Agnini, C., Anagnostou, E., et al. (2020). An astronomically dated record of Earth's climate and its predictability over the last 66 million years. *Science*, *369*(6509), 1383–1387. https://doi.org/10.1126/science.aba6853

Whipple, K. X. (2009). The influence of climate on the tectonic evolution of mountain belts. *Nature Geoscience*, *2*(2), 97–104. https://doi.org/10.1038/ngeo413

Wilcken, K. M., Codilean, A. T., Fülöp, R.-H., Kotevski, S., Rood, A. H., Rood, D. H., et al. (2022). Accelerator mass spectrometry of Be-10 and Al-26 at low nuclide concentrations. *Geochronology*, *4*(1), 339–352. https://doi.org/10.5194/gchron-4-339-2022

Wilcken, K. M., Fink, D., Hotchkis, M., Garton, D., Button, D., Mann, M., et al. (2017). Accelerator mass spectrometry on SIRIUS: New 6 MV spectrometer at ANSTO. *Nuclear Instruments and Methods in Physics Research Section B: Beam Interactions with Materials and Atoms*, *406*, 278–282. https://doi.org/10.1016/j.nimb.2017.01.003

Wilcken, K. M., Fujioka, T., Fink, D., Fülöp, R.-H., Codilean, A. T., Simon, K., et al. (2019). SIRIUS performance: Be-10, Al-26 and Cl-36 measurements at ANSTO. *Nuclear Instruments and Methods in Physics Research Section B: Beam Interactions with Materials and Atoms*, *455*, 300–304. https://doi.org/10.1016/j.nimb.2019.02.009

Willenbring, J. K., & Jerolmack, D. J. (2016). The null hypothesis: Globally steady rates of erosion, weathering fluxes and shelf sediment accumulation during Late Cenozoic mountain uplift and glaciation. *Terra Nova*, *28*(1), 11–18. https://doi.org/10.1111/ter.12185

Willenbring, J. K., & Von Blanckenburg, F. (2010). Long-term stability of global erosion rates and weathering during late-Cenozoic cooling. *Nature*, *465*(7295), 211–214. https://doi.org/10.1038/nature09044

Willett, S. D., & Brandon, M. T. (2013). Some analytical methods for converting thermochronometric age to erosion rate. *Geochemistry, Geophysics, Geosystems*, *14*(1), 209–222. https://doi.org/10.1029/2012gc004279

Windley, B. F., Alexeiev, D. V., Xiao, W., Kröner, A., & Badarch, G. (2007). Tectonic models for accretion of the Central Asian Orogenic belt. *Journal of the Geological Society, London*, *164*(1), 31–47. https://doi.org/10.1144/0016-76492006-022

Windley, B. F., Allen, M. B., Zhang, C., Zhao, Z. T., & Wang, G. R. (1990). Paleozoic accretion and Cenozoic re-deformation of the Chinese Tien Shan range, Central Asia. *Geology*, *18*(2), 128–131. https://doi.org/10.1130/0091-7613(1990)018<0128:PAACRO>2.3.CO;2

Wu, F., Fang, X., Yang, Y., Dupont-Nivet, G., Nie, J., Fluteau, F., et al. (2022). Reorganization of Asian climate in relation to Tibetan Plateau uplift. *Nature Reviews Earth & Environment*, *3*(10), 684–700. https://doi.org/10.1038/s43017-022-00331-7

Zech, R. (2012). A late Pleistocene glacial chronology from the Kitschi-Kurumdu Valley, Tien Shan (Kyrgyzstan), based on ^{10}Be surface exposure dating. *Quaternary Research*, *77*(2), 281–288. https://doi.org/10.1016/j.yqres.2011.11.008

Zhang, P., Molnar, P., & Downs, W. R. (2001). Increased sedimentation rates and grain sizes 2–4 Myr ago due to the influence of climate change on erosion rates. *Nature*, *410*(6831), 891–897. https://doi.org/10.1038/35073504

Zhao, X., Zhang, H., Lv, H., Lü, Y., Li, X., Liu, K., et al. (2021). Signatures of tectonic-climatic interaction during the Late Cenozoic orogenesis along the northern Chinese Tian Shan. *Basin Research*, *33*(1), 291–311. https://doi.org/10.1111/bre.12466

Zomer, R. J., Xu, J., & Trabuco, A. (2022). Version 3 of the global aridity index and potential evapotranspiration database. *Scientific Data*, *9*(1), 409. https://doi.org/10.1038/s41597-022-01493-1

Zubovich, A. V., Wang, X. Q., Scherba, Y. G., Schelochkov, G. G., Reilinger, R., Reigber, C., et al. (2010). GPS velocity field for the Tien Shan and surrounding regions. *Tectonics*, *29*(6). https://doi.org/10.1029/2010TC002772

References From the Supporting Information

Chang, J., Glorie, S., Qiu, N., Min, K., Xiao, Y., & Xu, W. (2021). Late Miocene (10.0~6.0 Ma) rapid exhumation of the Chinese south Tianshan: Implications for the timing of aridification in the Tarim basin. *Geophysical Research Letters*, *48*(3), e2020GL090623. https://doi.org/10.1029/2020GL090623

Chapman, J. B., Carrapa, B., Ballato, P., DeCelles, P. G., Worthington, J., Oimahmadov, I., et al. (2017). Intracontinental subduction beneath the Pamir Mountains: Constraints from thermokinematic modeling of shortening in the Tajik fold-and-thrust belt. *Bulletin*, *129*(11–12), 1450–1471. https://doi.org/10.1130/B31730.1

Chen, Z. L., Li, L., Jian, L., Hongliang, G., Rongbao, J., Shengxiang, L., et al. (2008). Preliminary study on the uplifting-exhumation process of the western Tianshan range, northwestern China. *Acta Petrologica Sinica*, *24*(4), 625–636.

Chen, Z. L., Wan, J. L., Liu, J., Li, S. X., & Zhen, E. J. (2006). Multi-stage uplift and exhumation of the west Tianshan Mountain: Evidence from the apatite fission-track dating. *Acta Geoscientia Sinica*, *27*(2), 97.

Chu, Z., Yu, X., Wang, Z., Xiao, W., Chen, Z., Han, S., & Yang, X. (2016). A comparison of uplifting history between Tianshan Mountains in China and Kyrgyz: Insights from fission track chronology. *Geology in China*, *43*(4), 1248–1257. (in Chinese with English abstract).

De Grave, J., Glorie, S., Buslov, M. M., Izmer, A., Fournier-Carrie, A., Batalev, V. Y., et al. (2011). The thermo-tectonic history of the Song-Kul plateau, Kyrgyz Tien Shan: Constraints by apatite and titanite thermochronometry and zircon U/Pb dating. *Gondwana Research*, *20*(4), 745–763. https://doi.org/10.1016/j.gr.2011.03.011

De Grave, J., Glorie, S., Ryabinin, A., Zhimulev, F., Buslov, M. M., Izmer, A., et al. (2012). Late Palaeozoic and Meso-Cenozoic tectonic evolution of the southern Kyrgyz Tien Shan: Constraints from multi-method thermochronology in the Trans-Alai, Turkestan-Alai segment and the southeastern Ferghana basin. *Journal of Asian Earth Sciences*, *44*, 149–168. https://doi.org/10.1016/j.jseaes.2011.04.019

De Pelsmaeker, E., Glorie, S., Buslov, M. M., Zhimulev, F. I., Poujol, M., Korobkin, V. V., et al. (2015). Late-Paleozoic emplacement and Meso-Cenozoic reactivation of the southern Kazakhstan granitoid basement. *Tectonophysics*, *662*, 416–433. https://doi.org/10.1016/j.tecto.2015.06.014

Du, Z. L., & Wang, Q. C. (2007). Mesozoic and Cenozoic uplifting history of the Tianshan region: Insight from apatite fission track. *Acta Geologica Sinica*, *81*(8), 1081–1101.

Dumitru, T. A., Zhou, D., Chang, E. Z., Graham, S. A., Hendrix, M. S., Sobel, E. R., & Carroll, A. R. (2001). *Uplift, exhumation, and deformation in the Chinese Tian Shan* (pp. 71–100). Memoirs-Geological Society of America. https://doi.org/10.1130/0-8137-1194-0.71

Glorie, S., Otasevic, A., Gillespie, J., Jepson, G., Danišík, M., Zhimulev, F. I., et al. (2019). Thermo-tectonic history of the Junggar Alatau within the Central Asian Orogenic belt (SE Kazakhstan, NW China): Insights from integrated apatite U/Pb, fission track and (U–Th)/He thermochronology. *Geoscience Frontiers*, *10*(6), 2153–2166. https://doi.org/10.1016/j.gsf.2019.05.005

Guo, Z. J., Zhang, Z. C., Wu, C. D., Fang, S. H., & Zhang, R. (2006). The Mesozoic and Cenozoic exhumation history of Tianshan and comparative studies to the Junggar and Altai mountains. *Acta Geologica Sinica*, *80*(1), 1–15.

He, Z., Wang, B., Su, W., Glorie, S., Ni, X., Liu, J., et al. (2022). Meso-Cenozoic thermo-tectonic evolution of the Yili block within the Central Asian Orogenic Belt (NW China): Insights from apatite fission track thermochronology. *Tectonophysics*, *823*, 229194. https://doi.org/10.1016/j.tecto.2021.229194

Jepson, G., Glorie, S., Konopelko, D., Gillespie, J., Danišík, M., Evans, N. J., et al. (2018a). Thermochronological insights into the structural contact between the Tian Shan and Pamirs, Tajikistan. *Terra Nova*, *30*(2), 95–104. https://doi.org/10.1111/ter.12313

Jepson, G., Glorie, S., Konopelko, D., Mirkamalov, R., Danišík, M., & Collins, A. S. (2018b). The low-temperature thermo-tectonic evolution of the western Tian Shan, Uzbekistan. *Gondwana Research*, *64*, 122–136. https://doi.org/10.1016/j.gr.2018.08.003

Jia, Y., Shen, X., Lü, L., Wang, Y., & Pang, J. (2023). Reconstruction of the Meso-Cenozoic tectono-geomorphological evolution of the Keguqin mountain in the Central Tian Shan based on geomorphological analysis and low-temperature thermochronology. *Tectonophysics*, *847*, 229685. https://doi.org/10.1016/j.tecto.2022.229685

Jia, Y., Sun, J., & Lü, L. (2020). Late Cenozoic tectono-geomorphologic evolution of the northern Tian Shan mountain range: Insight from U-Pb ages of detrital zircon grains from the Upper Oligocene-Quaternary sediments of the southern Junggar basin. *Journal of Asian Earth Sciences*, *194*, 104286. https://doi.org/10.1016/j.jseaes.2020.104286

Käßner, A., Ratschbacher, L., Jonckheere, R., Enkelmann, E., Khan, J., Sonntag, B. L., et al. (2016). Cenozoic intracontinental deformation and exhumation at the northwestern tip of the India-Asia collision—Southwestern Tian Shan, Tajikistan, and Kyrgyzstan. *Tectonics*, *35*(9), 2171–2194. https://doi.org/10.1002/2015TC003897

Käßner, A., Ratschbacher, L., Pfänder, J. A., Hacker, B. R., Zack, G., Sonntag, B. L., et al. (2017). Proterozoic–mesozoic history of the Central Asian orogenic belt in the Tajik and southwestern Kyrgyz Tian Shan: U-Pb, $^{40}Ar/^{39}Ar$, and fission-track geochronology and geochemistry of granitoids. *GSA Bulletin*, *129*(3–4), 281–303. https://doi.org/10.1130/B31466.1

Lü, H., Chang, Y., Wang, W., & Zhou, Z. (2013). Rapid exhumation of the Tianshan Mountains since the early Miocene: Evidence from combined apatite fission track and (U-Th)/He thermochronology. *Science China Earth Sciences*, *56*(12), 2116–2125. https://doi.org/10.1007/s11430-013-4715-1

Ma, Q., Shu, L. S., & Zhu, W. B. (2006). Mesozoic-cenozoic burial, uplift and exhumation: A profile along the Urumqi-Korla highway in the Tianshan mountains. *Xinjiang Geology*, *24*(2), 99–104.

Mohadjer, S., Ehlers, T. A., Bendick, R., Stübner, K., & Strube, T. (2016). A Quaternary fault database for central Asia. *Natural Hazards and Earth System Sciences*, *16*(2), 529–542. https://doi.org/10.5194/nhess-16-529-2016

Nachtergaele, S., De Pelsmaeker, E., Glorie, S., Zhimulev, F., Jolivet, M., Danišík, M., et al. (2018). Meso-Cenozoic tectonic evolution of the Talas-Fergana region of the Kyrgyz Tien Shan revealed by low-temperature basement and detrital thermochronology. *Geoscience Frontiers*, *9*(5), 1495–1514. https://doi.org/10.1016/j.gsf.2017.11.007

Nishiizumi, K. (2004). Preparation of ^{26}Al AMS standards. *Nuclear Instruments and Methods in Physics Research Section B: Beam Interactions with Materials and Atoms*, *223*, 388–392. https://doi.org/10.1016/j.nimb.2004.04.075

Rolland, Y., Jourdon, A., Petit, C., Bellahsen, N., Loury, C., Sobel, E. R., & Glodny, J. (2020). Thermochronology of the highest central Asian massifs (Khan Tengri-Pobedi, SE Kyrgyztan): Evidence for late Miocene (ca. 8 Ma) reactivation of Permian faults and insights into building the Tian Shan. *Journal of Asian Earth Sciences*, *200*, 104466. https://doi.org/10.1016/j.jseaes.2020.104466

Shen, C. B., Mei, L. F., Zhang, S. W., Liu, L., Tang, J. G., Zhou, F., et al. (2008). Fission-track dating evidence on space-time difference of Mesozoic-Cenozoic uplift of the Yilianhabierga mountain and Bogeda mountain. *Journal of Mineralogy and Petrology*, *28*(2), 63–70.

Song, M. C., Zhou, J. B., Song, Y. X., Wang, B., Li, S. Y., Li, J., & Wang, S. S. (2020). Mesozoic Weideshan granitoid suite and its relationship to large-scale gold mineralization in the Jiaodong Peninsula, China. *Geological Journal*, *55*(8), 5703–5724. https://doi.org/10.1002/gj.3607

Wang, Q., Li, S., & Du, Z. (2009). Differential uplift of the Chinese Tianshan since the Cretaceous: Constraints from sedimentary petrography and apatite fission-track dating. *International Journal of Earth Sciences*, *98*(6), 1341–1363. https://doi.org/10.1007/s00531-009-0436-2

Wang, Y., Cai, K., Sun, M., Xiao, W., De Grave, J., Wan, B., & Bao, Z. (2018). Tracking the multi-stage exhumation history of the western Chinese Tianshan by apatite fission track (AFT) dating: Implication for the preservation of epithermal deposits in the ancient orogenic belt. *Ore Geology Reviews*, *100*, 111–132. https://doi.org/10.1016/j.oregeorev.2017.04.011

Wang, Y. B., Wang, Y., Liu, X., et al. (2001). Apatite fission-track records of Mesozoic and Cenozoic episodic reactivation of the Tianshan and west Kunlun mountains. *Regional Geology of China*, *20*, 94–99.

Yang, G., & Qian, X. L. (1995). Mesozoic-cenozoic uplift of the Tian Shan intraplate orogenic belt: Evidence from zircon and apatite fission track dating. *Acta Scientiarum Naturalium Universitatis Pekinensis*, *31*(4), 473–478.

Yang, S. F., Chen, H. L., Cheng, X. G., Xiao, A. C., Zhou, Y. Z., Lu, H. F., et al. (2003). Cenozoic uplifting and unroofing of southern Tien Shan, China. *Journal of Nanjing University (Natural Sciences)*, *39*, 1–8.

Yang, W., Li, J., Guo, Z., Jolivet, M., & Heilbronn, G. (2017). New apatite fission-track ages of the western Kuqa depression: Implications for the Mesozoic–Cenozoic tectonic evolution of south Tianshan, Xinjiang. *Acta Geologica Sinica-English Edition*, *91*(2), 396–413. https://doi.org/10.1111/1755-6724.13107

Yin, J., Chen, W., Hodges, K. V., Xiao, W., Cai, K., Yuan, C., et al. (2018). The thermal evolution of Chinese central Tianshan and its implications: Insights from multi-method chronometry. *Tectonophysics*, *722*, 536–548. https://doi.org/10.1016/j.tecto.2017.11.037

Yu, Y., Chen, Y. S., Jian, H. C., Tang, Y. C., & Ning, J. Y. (2016). SKS wave splitting study of the transition zone at the central portion of the North China Craton. *Chinese Journal of Geophysics*, *59*(1), 141–151. https://doi.org/10.6038/cjg20160111

Zhang, B., Chen, W., Liu, J., Yin, J., & Sun, J. (2020). Thermochronological insights into the intracontinental orogeny of the Chinese western Tianshan orogen. *Journal of Asian Earth Sciences*, *194*, 103927. https://doi.org/10.1016/j.jseaes.2019.103927

Zhang, Z., Zhu, W., Shu, L., Wan, J., Yang, W., Zheng, B., & Su, J. (2011). Multi-stage exhumation of the NE Tarim Precambrian bedrock, NW China: Constraints from apatite fission track thermochronology in the Kuluketage area. *Terra Nova*, *23*(5), 324–332. https://doi.org/10.1111/j.1365-3121.2011.01017.x

Zhang, Z., Zhu, W., Zheng, D., Zheng, B., & Yang, W. (2016). Apatite fission track thermochronology in the Kuluketage and Aksu areas, NW China: Implication for tectonic evolution of the northern Tarim. *Geoscience Frontiers*, *7*(2), 171–180. https://doi.org/10.1016/j.gsf.2015.08.007

Zhang, Z. C., Guo, Z. J., Wu, C. D., & Fang, S. H. (2007). Thermal history of the Jurassic strata in the Northern Tianshan and its geological significance, revealed by apatite fission-track and vitrinite-reflectance analysis. *Acta Petrologica Sinica*, *23*, 1683–1695.

Zhao, S., Chen, W., Zhang, B., Sun, J., Shen, Z., & Zhang, Y. (2020). Mesozoic and Cenozoic exhumation history and magmatic-hydrothermal events of the central Tianshan Mt. Range, NW China: Evidence from (U–Th)/He and 40Ar/39Ar dating. *Journal of Asian Earth Sciences*, *194*, 104057. https://doi.org/10.1016/j.jseaes.2019.104057